CENTRO DE INVESTIGACIONES
EN OPTICA, A.C.

“CLEANING OF METAL SURFACES BY LASER IRRADIATION; MATHEMATICAL MODELING AND EXPERIMENTAL ANALYSIS”

Thesis to obtain the degree of Master of Science (Optics)

Author: Harrison Wandera Okumu

Thesis Director: Dr. Martín Ortiz Morales

León · Guanajuato · México
April 2022

Final version. Includes changes suggested by reviewers

Abstract

Metal derusting by means of laser irradiation has attracted considerable attention in recent years. This is a non-invasive and rapid cleaning process that is superior to conventional abrasive treatments in terms of maintaining the surface structure and saving time. The main purpose of this study was to determine the optimal laser cleaning parameters such as power, pulse duration, frequency, and wavelength for high carbon steel (AISI 1095) and grey cast iron (ASTM A159). Two samples of each metal were cleaned using a 20 W pulsed fiber and 30 W carbon (IV) oxide lasers, from which the fiber laser was proposed. In addition, a mathematical model was developed in MatLab (2021 a) and ANSYS Workbench (2020 R2) using Finite Element Analysis to study the mechanism of laser-matter interaction and the effect of surface microstructure on the cleaning process. Both simulation and the experimental results were analogous. Raman spectroscopy revealed the presence of hematite, goethite, siderite, wuestite, lepidocrocite, and ferrihydrite in uncleaned carbon steel. Hematite, goethite, and lepidocrocite were found in uncleaned grey cast iron. Scanning Electron Microscopy revealed cracks of about 2 μm and 3 μm wide on the surfaces of uncleaned carbon steel and grey cast iron respectively. SEM analysis of the most cleaned samples indicated no cracks on the surface. Additionally, Raman analysis showed the presence of amorphous carbon on the most cleaned samples which were later found to be protective against potential re-oxidation once they are exposed to the ambient environment. Energy Dispersive Spectroscopy indicated a significant drop in oxide composition from 19 to 2.3 % and 44.7 to 3.2 % in uncleaned and best-cleaned samples of carbon steel and grey cast iron respectively. Perspectives for future research works aimed at improving the vast field of laser cleaning are also discussed.

Dedication

To my beloved son, Alvin Trevor

Declaration

I solemnly certify that this study is all my own. All the experiments and results presented have not been conducted either at Centro de Investigaciones en Óptica, A.C. or any other accredited academic institution for the acquisition of either undergraduate or postgraduate qualification.

19/04/2022

Student's Sign

Date

First Examiner:

Dr. Martin Ortiz Morales

Second Examiner:

Dr. Claudio Frausto Reyes

Third Examiner:

Dr. Manuel H. De la Torre Ibarra

Acknowledgement

Special thanks go to Dr. Martin Ortiz Morales for his selfless role played in supervising this project and guaranteeing its success. His much-needed support was steadfast.

More thanks to all my coursework teachers who expeditiously demonstrated a high level of professionalism in administering theoretical aspects that were very instrumental in my practical work.

The role played by Dr. Claudio Frausto Reyes in equipping me with the necessary skills to handle Raman spectroscopic analysis can't go unnoticed. His guidance was ramified with zeal and resilience.

To Juan Sarabia Torres who came in handy during the preparation of experimental samples, I say thank you. The success of this project could not have been feasible without his priceless support.

I also highly acknowledge my assessors for the commitment dedicated towards revising this document with an aim of ensuring that all the work presented here bears a significant contribution to the scientific world. These include Dr. Martin Ortiz Morales, Dr. Claudio Frausto Reyes, and Dr. Manuel H. De la Torre Ibarra.

More special appreciation to CONACYT and the Mexican government for financially supporting my academic quest and ensuring my comfortable stay far from my family. The success attained in this academic program could not be a possibility without the support received.

More thanks to God for the gift of life and a healthy sustenance.

Contents

Abstract **ii**

Acknowledgement **vi**

List of Figures **xiv**

List of Tables **xvi**

1 Introduction **1**

1.1 Traditional Methods of Rust Cleaning 1

1.2 Laser Cleaning 3

1.2.1 Dry Laser Cleaning (DLC) 3

1.2.2 Steam Laser Cleaning (SLC) 4

1.3 Research Gap 5

1.4 Research Objectives 5

2 Theoretical Background **7**

2.1 Introduction 7

2.2 Lasers 7

2.2.1 The Principle of Lasing 8

2.2.2 Types of Lasers 9

2.2.2.1 Liquid Lasers 9
2.2.2.2 Gas Lasers 10
2.2.2.3 Solid-State Lasers 16
2.2.3 Laser Operational Modes 20
2.3 Laser-Matter Interaction 21
2.3.1 Thermodynamic Effects 21
2.3.2 The Mechanism of Melting and Solidification 22
2.3.3 Gasification and Ionization 22
2.3.4 Explosion of the Phase 23
2.4 Optical Properties of Metals 24
2.5 Fundamental Parameters for Laser Cleaning 25
2.6 Laser Machining 26

3 Methodology **27**

3.1 Introduction 27
3.2 Properties of Carbon Steel 28
3.2.1 Chemical Properties 29
3.2.2 Physical Properties 29
3.2.3 Thermal Properties 29
3.2.4 Effects of Corrosion on Carbon Steel 30
3.3 Properties of Grey Cast Iron 30
3.3.1 Chemical Properties 31
3.3.2 Thermal Properties 31
3.3.3 Mechanical Properties 32

3.3.4 Physical Properties 32

3.3.5 Effects of Corrosion on Grey Cast Iron 32

3.4 Experimental Methodology 33

3.4.1 Focusing the Laser Beam 33

3.4.1.1 The Working Principle of F-theta Lens 33

3.4.1.2 The Working Principle of the Galvanometer Scanning Head 34

3.5 Characterization of the Samples 36

3.6 Mathematical Simulation to Demonstrate Heat Distribution During Cleaning of Carbon Steel and Cast Iron 37

4 Results Analysis and Discussion **41**

4.1 Introduction 41

4.2 Experimental Results 42

4.2.1 Carbon (IV) Oxide Laser 42

4.2.2 Fiber Laser 43

4.2.3 Surface Morphology and Composition 45

4.2.3.1 Optical Microscopy 46

4.2.3.2 Scanning Electron Microscopy (SEM) 48

4.2.3.3 Raman Spectroscopy 53

4.2.4 Chemical Composition 59

4.2.4.1 Energy Dispersive X-ray Spectroscopy (EDS) 59

4.3 Simulation Results 61

4.3.1 Electron-Lattice Temperature Transition 61

4.3.2 Phase Change Material (PCM) 62

4.3.3 Surface Microstructure 64

4.3.4 Temperature and Depth of Penetration 65

4.3.5 Temperature and Time 66

4.3.6 Fluence and Depth of Penetration 66

5 Conclusions and Recommendation **69**

5.1 Conclusions 69

5.2 Recommendations for Future Work 71

Bibliography **72**

List of Figures

2.1 The lasing mechanism 8

2.2 Diagram of a three-level lasing action. 9

2.3 Laser system based on liquid crystals (Image courtesy of [49]) 10

2.4 Working mechanism of a CO_2 laser (Image courtesy of[55]). 11

2.5 A 50 W pulsed CO_2 laser with a wavelength of 10.6 μm (Image courtesy of CIO laser applications lab., Aguascalientes). 12

2.6 Three-level lasing mechanism of the nitrogen laser. 12

2.7 A nitrogen laser with a wavelength of 337 nm and 170 J pulse energy at 20 Hz (Image courtesy of [63]). 13

2.8 (a) A 68W KrF excimer laser with 750kHz repetition rate (Image courtesy of [69]), and (b) the working mechanism. 14

2.9 A 10 mW He-Ne Laser with a wavelength of 594 nm (Courtesy: CIO laser applications lab., Aguascalientes). 15

2.10 Levels of energy in a He-Ne laser (Image courtesy of [72]). 15

2.11 Ruby laser electronic transition. 17

2.12 Q-switch output pulse switching device for ruby lasers (Image courtesy of [78]). 17

2.13 Nd: YAG laser quantum transitions 18

2.14 An internal structure of the Nd: YAG laser (Image courtesy of [86]). . 19

2.15 Construction of a 1550 nm fiber laser. 19

2.16 A comparison between CW and pulsed operation. 21

2.17 The mechanism of melting and solidification. 22

2.18 Gasification and ionization process. 23

2.19 The process for the generation of phase explosions. 24

2.20 Absorptivity of laser energy versus wavelength for various metallic samples (Image courtesy of [109]). 26

3.1 Uncorroded hot-rolled carbon steel plates (image courtesy of [110]). . 29

3.2 Corroded carbon steel plate. 30

3.3 Uncorroded brake disk. 31

3.4 Corroded brake disk. 32

3.5 The working principle of an f-theta lens. 34

3.6 Galvanometer scanning head (a) X and Y mirror arrangement, and (b) working mechanism. 35

3.7 The set-up used for experimental laser cleaning (a) using the fiber laser, and (b) using CO_2 laser. 35

3.8 Laser scanning patterns used in the cleaning of carbon steel and cast iron (a) continuous, and (b) lineal. 36

3.9 Simulation process implemented in MatLab. 38

3.10 Simulation process implemented in ANSYS workbench. 39

4.1 Physical appearance of carbon steel samples (a) S_{c1}, (b) S_{c2}, and (c) S_{c3}. 43

4.2 Variation between average powers in Watts and percentage of the fiber laser used in experimental process. 44

4.3 Physical appearance of carbon steel samples (a) S_{f1}, (b) S_{f2}, and (c) S_{f3}. 44

4.4 Physical appearance of grey cast iron samples (a) R_{f1}, (b) R_{f2}, and (c) R_{f3}. 45

4.5 Digital optical microscope in use [131] 46

4.6 Optical analysis of the carbon steel sample S_{f2} 46

4.7 Optical analysis of the carbon steel sample S_{f3} 47

4.8 Optical analysis of the uncleaned grey cast iron sample R_{f1} 47

4.9 Optical analysis of the less cleaned grey cast iron sample R_{f2} 48

4.10 Optical analysis of the most cleaned grey cast iron sample R_{f3} 48

4.11 SEM micrographs of carbon steel samples with (a) for S_{f1}, (b)for S_{f2}, and (c) for S_{f3}. 50

4.12 SEM micrographs of grey cast iron samples with (a) for R_{f1}, (b) for R_{f2}, and (c) for R_{f3}. 52

4.13 Raman spectrum of the uncleaned carbon steel sample S_{f1}. 54

4.14 Raman spectrum of the less cleaned carbon steel sample S_{f2}. 54

4.15 Raman spectrum of the most cleaned carbon steel sample S_{f3}. 55

4.16 Normalized Raman spectra of the carbon steel samples S_{f1}, S_{f2} and S_{f3}. 56

4.17 Raman spectrum of the uncleaned grey cast iron sample R_{f1}. 57

4.18 Raman spectrum of the less cleaned grey cast iron sample R_{f2}. 57

4.19 Raman spectrum of the most cleaned grey cast iron sample R_{f3}. . . . 58

4.20 Normalized Raman spectra of the grey cast iron samples R_{f1}, R_{f2} and R_{f3}. 59

4.21 Temperature transformation against time and ablation depth of the sample, (a) electron, and (b) lattice: numerical simulation of grey cast iron with laser wavelength of 1070 nm and fluence of 3.68 Jcm^{-2} 62

4.22 Phase transition of carbon steel during interaction with a laser pulse of wavelength 1070 nm and fluence of 6.44 Jcm^{-2}. 63

4.23 Phase transition of grey cast iron during interaction with a laser pulse of wavelength 1070 nm and fluence of 6.44 Jcm^{-2}. 63

4.24 Heat distribution on the surface of carbon steel; numerical simulation with a laser pulse of wavelength 1070 nm and fluence of 6.44 Jcm^{-2}. . 64

4.25 Heat distribution on the surface of grey cast iron; numerical simulation with a laser pulse of wavelength 1070 nm and fluence of 6.44 Jcm^{-2}. 64

4.26 Variation of temperature and depth of penetration at different periods of the laser pulse; simulation of carbon steel with a laser of wavelength 1070 nm and fluence of 6.44 Jcm^{-2}. 65

4.27 Variation of temperature and time at different depths of penetration; simulation of carbon steel with a laser of wavelength 1070 nm and fluence of 6.44 Jcm^{-2}. 66

4.28 Variation of ablation depth versus fluence; numerical simulation of carbon steel with a laser of wavelength 1070 nm and maximum fluence of 15 Jcm^{-2}. 66

4.29 Variation of ablation depth versus fluence; numerical simulation of grey cast iron with a laser of wavelength 1070 nm and maximum fluence of 15 Jcm^{-2}. 67

List of Tables

1.1 Traditional methods of rust cleaning [3–5]. 2

1.2 Comparison between DLC and SLC cleaning techniques. 5

2.1 Characteristics of gases used in excimer lasers [67, 68]. 14

2.2 Transition-based He-Ne lasers [73]. 16

3.1 Chemical composition of carbon steel AISI 1095. 29

3.2 Physical properties of carbon steel AISI 1095. 29

3.3 Thermal properties of carbon steel AISI 1095. 30

3.4 Chemical composition of cast iron ASTM A159. 31

3.5 Thermal properties of cast iron ASTM A159. 31

3.6 Mechanical properties of grey cast iron ASTM A159. 32

3.7 Physical properties of grey cast iron ASTM A159 32

3.8 Laser parameters used in the simulation process [124, 125] 39

3.9 Material parameters used in the simulation process [126–129] 40

4.1 Experimental CO_2 laser parameters used for the cleaning of carbon steel samples. 42

4.2 Experimental fiber laser parameters used for the cleaning of carbon steel samples. 43

4.3 Experimental fiber laser parameters used for the cleaning of cast iron samples. 45

4.4 X-ray diffraction spectroscopy (EDS) of carbon steel samples S_{f1}, S_{f2}, and S_{f3}. 59

4.5 Elemental ratios of the carbon steel samples S_{f1}, S_{f2}, and S_{f3}. 60

4.6 X-ray diffraction spectroscopy (EDS) of grey cast iron samples R_{f1}, R_{f2}, and R_{f3}. 61

4.7 Elemental ratios of the cast iron samples R_{f1}, R_{f2}, and R_{f3}. 61

4.8 Comparison between simulation and experimental values of fluence and ablation depth of carbon steel samples. 67

4.9 Comparison between simulation and experimental values of fluence and ablation depth of grey cast iron samples. 68

Chapter 1

Introduction

Environmental exposure of metals causes oxidation and subsequent deterioration, otherwise known as rust. This is due to the reaction between the metal and oxygen in the presence of moisture [1]. The mechanisms of degradation change based on the kind of material. The loss of properties in polymers is called degradation. The process of corrosion is mostly experienced in iron metals and their alloys such as stainless steel, carbon steel, cast iron, and many others. Rust has a chemical formula of $Fe_2O_3 \cdot nH_2O$ and $(FeO(OH) \cdot Fe(OH)_3)$ [2]. Over a significant period, the entire metal may totally deteriorate, hence the need for cleaning.

1.1 Traditional Methods of Rust Cleaning

Rust cleaning from metal surfaces considering non-invasive methods has been a subject of discussion for decades. Many traditional methods including the use of vinegar, steel wool, sandblasting, acid pickling, among others have been in use for many decades. Some of these methods have been described in **Table 1.1**.

Table 1.1: Traditional methods of rust cleaning [3–5].

Method	Advantages	Disadvantages
1. Sandblasting	• Less mechanical sophistication. • Diversified use. • Blasting particles can penetrate hidden areas.	• Risk of accident due to falling sand particles. • High risk of damaging the surface during cleaning process. • Time consuming. • The smallest size of particle that can be cleaned is ≈ 4.5 μm.
2. Use of white vinegar	• Less laborious. • Less skills required. • Affordable.	• Environmental pollution. • Time consuming. • Risk of damaging the material due to corrosive nature of the vinegar. • Requires several liters of vinegar to clean large volume pieces.
3. Use of steel wool	• Relatively affordable. • Less skills required to clean. • Steel wool can be used in a variety of cleaning demands ranging from industrial to household.	• Causes surface wear. • Labor intensive. • Environmental pollution due to falling pieces of steel wool.

We notice that most of the traditional cleaning methods are not eco-friendly, requires more labor and cannot be applied in cases where large cleaning requirements are a necessity. Laser cleaning has therefore been considered one of the best options since it is a non-contact method, more efficient, and environmentally friendly [6].

1.2 Laser Cleaning

Since invention of the first laser in the early 1960s [7], different interdisciplinary applications have emerged. Some of these applications are industrial [8], marking [9, 10], medicine [11], communication [12], military [13], among others. Laser cleaning is one of the least explored areas due to many different parameters to be controlled. The parameters include average power, rate of pulses, spot size, scan speed, number of passes, and spacing between contiguous lines. The concept of laser cleaning has been in existence from early 1980s [14]. There are two main methods involved; dry and steam laser cleaning [15].

1.2.1 Dry Laser Cleaning (DLC)

The dry laser cleaning (DLC) approach is based on one-dimensional temperature rise of the sample, demonstrates that cleaning efficacy is significantly dependent on the laser pulse shape [16]. In this case, a sample is exposed directly to the laser beam and scanned several times (depending on the level of rust) until the surface is melted and ablated. During the recent decade, the approach has gained in popularity. Circuit board printing [17], Random Access Memory (RAM) manufacture [18], lithography [19], and epitaxial growth [20] are among the industrial fields that have employed the DLC technique.

Labuschagne and co-workers [21] studied the threshold damage caused by the Nd: YAG laser during paint removal from 316L stainless steel. From the 20^{th} pulse, surface discoloration developed owing to increasing irradiation. The condition changed when the fluence was raised, and discoloration occurred at a smaller number of pulses. In 2018 (Mohammed K. *et al.*) [22] incorporated the use of Nd: YAG laser in coat removal from automotives. On most occasions, laser cleaning was proven to be superior to traditional chemical stripping techniques. In 2019 (Antonopoulou N. *et al.*) [23] developed both theoretical and experimental rust removal approaches from coins using Nd: YAG laser with Q-switching. The laser cleaning feasibility of copper, silver, and other metal alloys was revealed in this research. More laser energy was required to ablate rust from highly corroded coins compared to less corroded ones.

In 2005 (Oltra R. *et al.*) [24] examined the impact of pulse duration, fluence, and repetition rate of an Nd: YAG laser in paint removal. It was noted that the best ablation efficiency was reached at the maximum repetition rate. On the other hand,

a pulse duration of 5 ns was found to produce less ablation efficiency compared to 100 ns. In 2018 (Narayanan V. *et al.*) [25] conducted an experimental study to investigate the surface effects caused by a 30 W fiber laser cleaning of rust from mild steel. It was revealed that, as the number of scans and laser power rose, the depth of ablation increased but decreased when the scan speed increased. Scan pattern was also found to significantly influence the surface roughness of the cleaned samples.

1.2.2 Steam Laser Cleaning (SLC)

This technique involves condensing some vapor of a given liquid (e.g water) on the sample's surface before ablating it with a laser pulse, almost instantly [26]. The vapor penetrates 'hidden' sections of the surface microstructure and with the aid of incoming laser pulse, a recoil pressure builds up, ablating the rust. In 1992 (Andrew T. *et al.*) [27] demonstrated SLC of silicon membrane stencil mask by water vapor and UV-excimer laser. Results indicated a high particle ablation with less energy compared to DLC technique that had been performed a year before using the same laser. In 1991 (Susan A. *et al.*) [28] cleaned silicon substrates using a carbon (IV) oxide laser but the achieved efficiencies were found to be much less compared to the one achieved using UV-excimer laser. In 2002 (Zapka *et al.*) [29] used a pulsed Er: YAG laser and obtained similar results as those found by Susan and coworkers.

In 1999 (Mosbacher *et al.*) [30] did a comparison of nanosecond and picosecond steam laser cleaning of silicon wafers. Thresholds of 50 mJ/cm^2 and 20 mJ/cm^2 were proposed for ns and ps lasers respectively, which represented a greater than 90 % of cleaning efficiency in comparison to their respective DLC. In 1998 (Zhang Y. *et al.*) [31] developed both theoretical and experimental SLC and DLC to investigate the effect of wavelength and fluence on the cleaning efficiency. It was found that, cleaning efficiency increased with decrease in wavelength and increase in fluence. Other works conducted in this field included removal of sub-micron down to nano-particles by use of infrared laser [32], and effect of vapor thickness on the cleaning efficiency [33].

The comparison between SLC and DLC is given in **Table 1.2**. The comparison is based on the application of both techniques using the CO_2 laser in different experimental regions (Germany and Singapore) [28].

Table 1.2: Comparison between DLC and SLC cleaning techniques.

DLC	SLC
1. High cleaning threshold.	1. Low cleaning threshold.
2. Largely depends on humidity inside the laboratory where the experiments are being carried out.	2. Particles are detached by the rapid vaporization of the surface liquid.
3. Cleaning efficiency is influenced by the melting of the surfaces.	3. Cleaning efficiency is influenced by the vaporization of the surface liquid.
4. There is a direct interaction between the sample and the laser pulse which poses the risk of damaging the sample if the cleaning parameters are not meticulously selected.	4. The sample is indirectly heated through the liquid film on the surface which limits the chances of damaging the sample.
5. Cleaning efficiency increases with an increase in humidity inside the laboratory where the cleaning is being conducted.	5. Cleaning efficiency does not depend on the humidity since the liquid vapor is availed by the laser system.

In this research however, the DLC technique was used to conduct our experimental process due to its less sophistication which makes it economical to set up.

1.3 Research Gap

After intensive bibliographic research, we established that the influence of surface microstructure to the efficiency of laser cleaning has not been addressed. The concept of surface passivation against future re-oxidation after laser cleaning has also not been investigated.

1.4 Research Objectives

The main objective of this research work is to determine the laser irradiation parameters that will give the most significant effect in the laser cleaning of metal parts and the control of surface effects related to laser parameters.

Other objectives include to:

- determine through bibliographic research, the types of lasers to be used, the

type of interaction required, as well as the current methodologies and techniques for cleaning the metal surfaces,

- determine the type of oxides formed in different materials,
- determine the type of metallic material,
- determine the laser parameters suitable for cleaning metal surfaces, and
- evaluate the cleanliness of metal surfaces using characterization techniques.

Chapter 2

Theoretical Background

2.1 Introduction

Understanding the theoretical framework of the laser cleaning process is essential to gaining a glimpse of the physics involved. Since this research involves laser cleaning of metallic samples, much of the concepts discussed in this chapter are based on a broad spectrum of laser-matter interaction in metals.

2.2 Lasers

The earliest works in the field of lasers were pioneered by Einstein in the year 1917 inspired by the ideologies of probability coefficients derived from Planck's law of radiation [34]. Over the years, more scientists emerged providing both theoretical and practical aspects to culminate the works developed by Einstein. For instance, in the year 1928, *R.W. Ladenburg* theoretically illustrated negative absorption and stimulated emission [35].

In the year 1947, *R.C. Rutherford* and *W.C. Lamb* demonstrated experimentally the works developed by *Ladenburg* [36]. Furthermore, in the year 1950, *Alfred Kastler* proposed optical pumping which he later demonstrated practically in collaboration with *Brossel* and *Winter* in 1952 [37]. Almost a decade later, in the year 1960, *Theodore Maiman* was able to design the first fully functional laser using the ideas that had been developed by the previous scientists. The pumping medium was made of ruby crystal and was able to radiate a red laser with a wavelength of approximately 694 nm [38, 39].

2.2.1 The Principle of Lasing

The acronym LASER stands for "Light Amplification by Stimulated Emission of Radiation" [40]. Contrary to other light sources, lasers are specially designed to emit light that is coherent, monochromatic, unidirectional, and with high intensity. A lasing system is made up of dedicated components that operate relatively to ensure a smooth and steady optical emission. These include the active medium, optical resonator and pumping source [41].

The active medium (also called the gain medium), is made up of either solid, liquid, or gas that can amplify the stimulated optical beam that goes through it [42]. It may either be electrically or optically pumped depending on the type of laser.

The optical resonator (also called the optical cavity) is comprised of two highly reflective mirrors. One of the mirrors is partially reflective and therefore allows the amplified beam to pass through it. The optical cavity reflects the stimulated light beam to and fro' several times, producing amplification by the active medium as shown in the **Figure 2.1**.

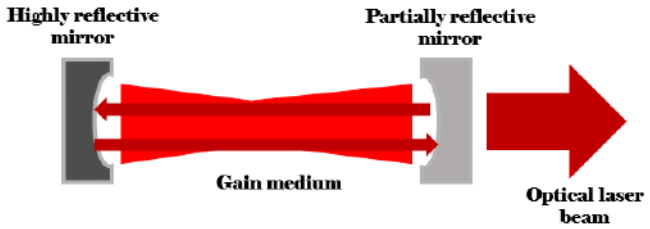

Figure 2.1: The lasing mechanism

As shown in **Figure 2.2**, the lasing action can be summarized as follows [43]:

- When energy is supplied to the gain medium, the electrons' energy level is raised to an unstable state.
- A metastable state, with a much longer lifespan and lower energy than the lower state, is formed when these atoms spontaneously decay.
- When the bulk of atoms are in metastable condition, a population inversion has occurred.
- A photon is produced when an electron returns to its ground state spontaneously.

– A cascading effect occurs when the electron induces the generation of another photon of the same wavelength.

– Photons are sent back through the medium along the lasing axis by the highly reflecting mirror and the slightly reflective mirror, which both contribute to the continuation of the reaction.

– As long as energy is supplied to the lasing medium, laser radiation will thrive.

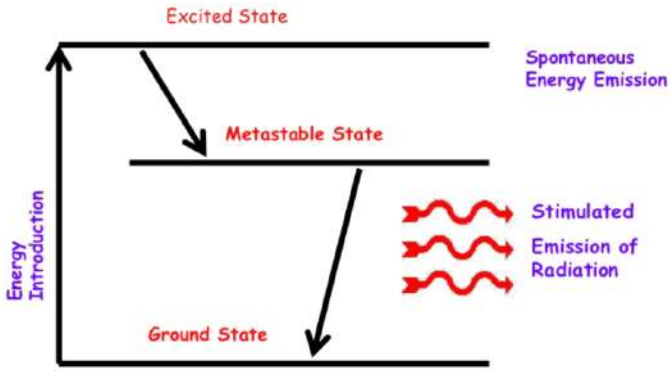

Figure 2.2: Diagram of a three-level lasing action.

2.2.2 Types of Lasers

Many types of lasers have been pioneered in the recent past. These lasers are classified into four major categories based on the nature of the active medium used. These include liquid, semiconductor, solid-state, and gas lasers [44, 45].

2.2.2.1 Liquid Lasers

These are lasers whose active medium is a liquid and optical signal is used as a source of energy [44]. A good example of the liquid laser is one that uses an organic dye as the active medium, and it is commonly referred to as **dye laser**. It is fabricated by a combination of an organic dye with a given solvent and the generated laser beam has a wavelength ranging from near UV to near IR regions of the electromagnetic spectrum [46, 47]. Examples include rhodamine (540–680 nm), fluorescein (530–560 nm), stilbene (410–480 nm), coumarin (490–620 nm), among others [48].

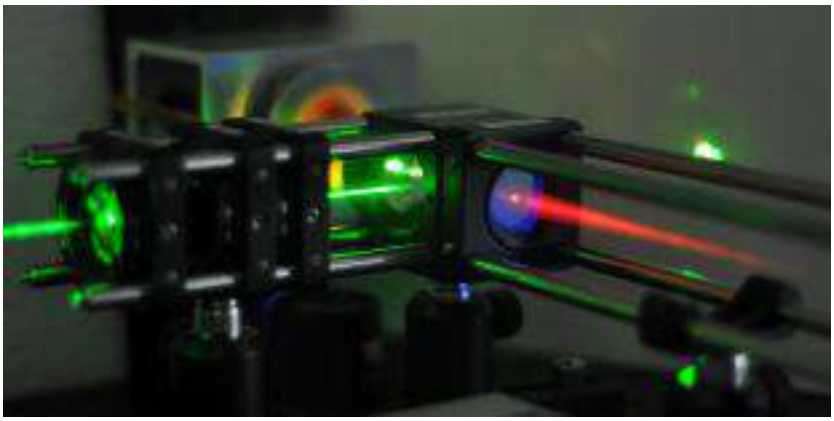

Figure 2.3: Laser system based on liquid crystals (Image courtesy of [49])

Dye lasers are quite flexible. Aside from their well-known wavelength agility, these lasers may provide huge, pulsed energy or average powers. They may produce hundreds of Joules for each pulse and average powers on a kilowatt scale [50]. Spectroscopy, atomic vapor laser isotope separation, astronomical star guidance, and manufacturing is just a few of the potential uses [51, 52].

2.2.2.2 Gas Lasers

These are lasers whose active medium is in a gaseous state [53]. In this case, the medium can be made of either one gas or a combination of gases. In his book, *Renk* described a detailed working mechanism and applications of various gas lasers which included excimer laser, He-Ne laser, CO_2 laser, metal vapor laser, optically pumped gas laser, among others [45]. However, for our case, we shall endeavor on a few of them that are closely related to our field of research.

(I). **Carbon (IV) Oxide (CO_2) Laser.**

Carbon (IV) oxide laser surpasses all previous CW lasers in terms of power [54]. However, it can also be operated as pulsed or transversely excited atmospheric (TEA). The conversion efficiency of electrical power to laser radiation is significantly higher $(10 - 20\%)$ compared to most gas lasers and operates within wavelengths of 9.6 and 10.6 μm as shown in **Figure 2.4**.

Vibrational states of nitrogen molecules are created when electrical current is applied to a gain medium. This vibrational energy will last for a long time since these molecules are made entirely of nitrogen. Carbon dioxide becomes a powerful amplifier for pumped energy once nitrogen molecules vibrate at high frequencies.

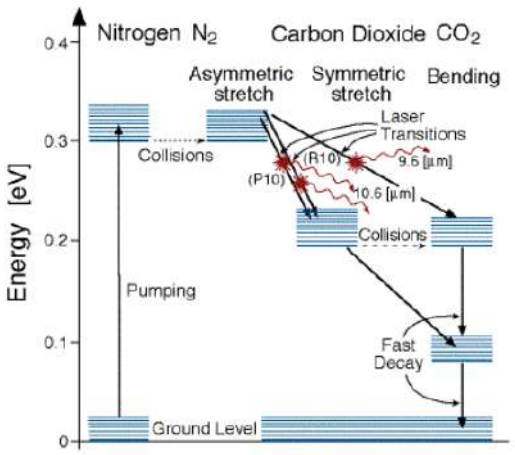

Figure 2.4: Working mechanism of a CO_2 laser (Image courtesy of[55]).

Heat is transferred to the helium when nitrogen molecules encounters helium atoms that are colder than their excited state. To sustain the population inversion with the excited CO_2 atoms, helium atoms must be cooled [56].

Advantages of CO_2 laser include [56, 57]:

- A few watts to 15 kilowatts of power may be achieved in CO2 laser system.
- It has a wide range of applications from industrial (for cutting, marking, and welding), medical (for dermatology), to military (for weaponry research). For instance, the CO_2 laser shown in the **Figure 2.5** was used during our experimental cleaning process in the lab.
- Boasts more than 20000 hours of service.
- In comparison to other gas lasers (e.g argon and He-Ne), it has a higher efficiency.
- It has a diverse waveform output format.

The drawbacks of CO_2 laser include:

- Purchasing one is a significant financial obligation.
- Because of its high-power consumption, it is expensive to operate and maintain.
- It is less absorbed by most metals limiting it's machinability especially in laser cleaning industry.

Figure 2.5: A 50 W pulsed CO_2 laser with a wavelength of 10.6 μm (Image courtesy of CIO laser applications lab., Aguascalientes).

(II). Nitrogen (N_2) Laser.

A vibronic laser prototype is the nitrogen laser [45]. The spacing between the nitrogen nuclei affect the electronic energy. N_2 contains both electrical and vibrational energy at its vibronic energy level which is given by [58];

$$E_{n,v} = E_n + \left(v + \frac{1}{2}\right) h\nu_{vib.} \tag{2.1}$$

whereby, $(v + 1/2)h\nu_{vib}$ represents vibrational energy, E_n the n^{th} state's electron energy, and ν_{vib} is the frequency of vibration.

Excitation of N_2 molecules to vibronic states is caused by the collision of electrons in a gas discharges. Electronic systems with n = 2 have their vibration levels heightened [59]. Laser near UV radiation is generated at the level-energies $E_{2,v}$. As a result, CW operation is impossible since the laser is self-terminating. Very low gas discharge pulses are suitable for pumping (duration 1 ns). The Franck–Condon principle governs optical transitions [60].

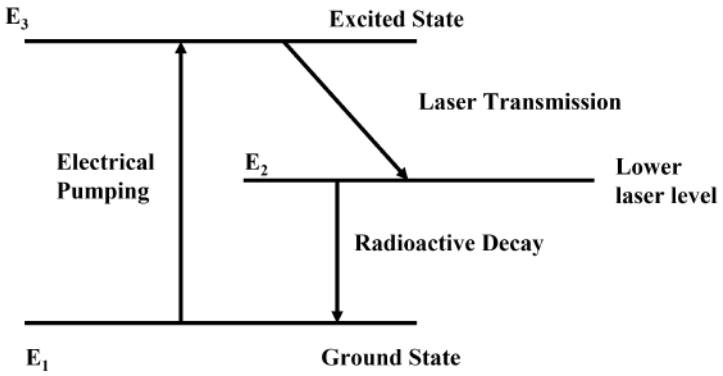

Figure 2.6: Three-level lasing mechanism of the nitrogen laser.

The drawbacks of N_2 laser include [61]:

- The Nitrogen laser's beam quality is poor.
- Its divergence is much larger than that of other lasers.
- It has a low power output.
- It has a low efficiency.

Some of the applications of N_2 laser include; dye laser pumping using transverse optical mechanism (like the one shown in **Figure 2.7**), measuring pollutants in the atmosphere (Lidar), Laser desorption/ionization aided by a matrix, laser cutting, among others [51, 62].

Figure 2.7: A nitrogen laser with a wavelength of 337 nm and 170 J pulse energy at 20 Hz (Image courtesy of [63]).

(III). **Excimer Laser.**

Nikolai Basov, Vladimir Danilychev, and Yu. M. Popov employed liquid xenon dimer (Xe_2) driven by a beam of electrons to detect a narrowing spectral line that appeared at 176 nm in 1971 [64]. Inspired by this discovery, a group of researchers in 1972 used xenon gas at high-pressure to better support the idea of stimulated emission. Mani Lal Bhaumik of Northrop Corporation in Los Angeles demonstrated for the first time in March 1973 a xenon excimer laser with wavelength of 173 nm and controlled by an electron beam [65].

As a buffer gas, neon is the most common choice for the active medium. 2–9 percent, 90–98 percent, and 0.2 percent of innert, buffer, and halogen gases respectively make up a standard excimer laser's gas combination [66]. The buffer gas is used to carry energy. An electric emission is used to stimulate the mixture in a pressure vessel

(3500–5000 mbar). XeCl, ArF, XeF, and KrF (shown in **Figure 2.8**) are examples of inert gas halides that have short lifetimes and are unstable in the ground state when combined with the gas mixture [67].

Table 2.1: Characteristics of gases used in excimer lasers [67, 68].

Gas	Wavelength (nm)	Remarks
XeCl	308	Mostly applied in marking. FDA authorized to treat psoriasis and vitiligo and certain inflammatory disorders.
ArF	193	High operating voltages are required to efficiently discharge energy. With respect to organic compounds, it has the smallest absorption depth.
XeF	351	Low absorption in polymers make this wavelength unsuitable for machining.
KrF	248	The most powerful and efficient excimer laser for machining polymers.

(a) **(b)**

Figure 2.8: (a) A 68W KrF excimer laser with 750kHz repetition rate (Image courtesy of [69]), and (b) the working mechanism.

(IV). **Helium-Neon (He-Ne) Laser.**

This laser uses a 10:1 combination of He:Ne as the gain medium inside a tiny elec-

trical discharge at a total pressure of roughly 1 torr [70]. The wavelength of the most well-known and widely used He-Ne laser is 632.8 nm (red region of the visible spectrum).

The first CW laser in the world was the He-Ne and it was invented by Bell Telephone Laboratories' Ali Javan, Bennett, and Herriott in 1961 [71]. They're the most common gas lasers. Among the most common uses of He-Ne lasers include optical alignment, spectroscopy, metrology, scanning bar-codes, holography, reading optical dics, and laser pointer. An example of He-Ne laser is shown in **Figure 2.9**.

Figure 2.9: A 10 mW He-Ne Laser with a wavelength of 594 nm (Courtesy: CIO laser applications lab., Aguascalientes).

He-Ne laser is electrically pumped. A current is used to excite electrons in the active medium of He-Ne gas. Atoms of helium are energized by electrons in a gas discharge and have an unusually extended life span as a result. Excited He and Ne atoms collide, and the excitation energy from He is transferred to Ne as shown in **Figure 2.10**.

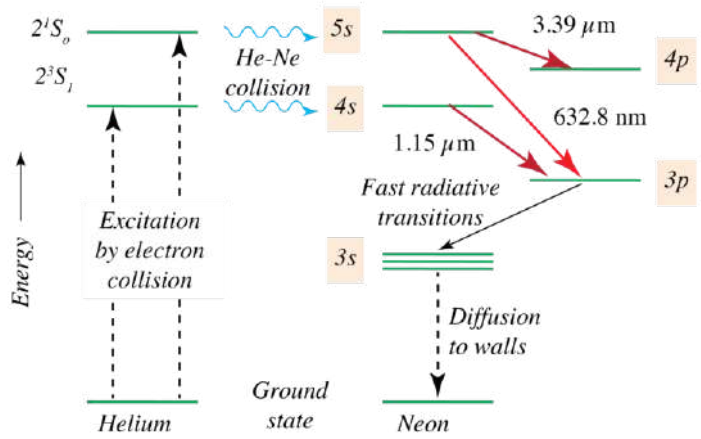

Figure 2.10: Levels of energy in a He-Ne laser (Image courtesy of [72]).

Laser beam of 632.8 nm is generated when $5s \rightarrow 3p$ transitions are stimulated. $3p \rightarrow$

$3s$ transitions depopulate 3p levels by spontaneous radiation ($\lambda \approx$450 nm). The 3s state interactions of neon atoms with the tube wall allow for relaxation; this is a non-radiative relaxation process. A thin gas tube is preferred for obtaining a sufficiently rapid relaxation. The 5s state has a lifespan of around 100 nanoseconds, while the 3p state has a lifetime of about 10 nanoseconds. Laser light with a wavelength of 3.39 μm is generated when $5s \rightarrow 4p$ transitions are stimulated. **Table 2.2** gives a summary of some of the most common He-Ne lasers based on lasing transitions.

Table 2.2: Transition-based He-Ne lasers [73].

Lasing Transition	**Wavelength (nm)**	**Color of the Observed Beam**
$2s_2 \rightarrow 2p_1$	1523.1	Infrared
$3s_2 \rightarrow 2p_2$	640.1	Red
$3s_2 \rightarrow 2p_7$	604.6	Orange
$3s_2 \rightarrow 2p_{10}$	543.5	Green

2.2.2.3 Solid-State Lasers

Solid-state lasers employ a solid gain medium instead of a liquid or gas [74]. Although semiconductor-based lasers are solid-state, they are typically recognized as a different class. In this case, we shall briefly discuss a few types which include ruby laser, YAG laser, and fiber laser. Of more interest will be the fiber laser since one of its applications was extensively utilized in our research.

(I). **Ruby Laser.**

At Hughes Research Laboratories, Theodore H. Ted Maiman built the world's first operating laser utilizing a ruby crystal on May 16, 1960 [39, 75]. Ruby lasers produce coherent visible light pulses at 694.3 nm (bright red color).

A ruby laser utilizes Cr^{3+} ions doped with 0.05 % by weight of Cr_2O_3 in an Al_2O_3 (sapphire) crystal; the density of Cr^{3+} ions is $N_0 = 1.61025\ m^3$ [76]. Two long-lived energy states of an excited Cr^{3+} ion exist in Al_2O_3. The levels have a radiation lifetime of approximately 3 ms. Pumping requires two broad energy bands as shown in **Figure 2.11**. A pair of slightly different wavelengths are used to optically transition between the long-lived and ground states. The impurity (Cr^{3+} ions) in sapphire have trigonal and cubic crystalline fields.

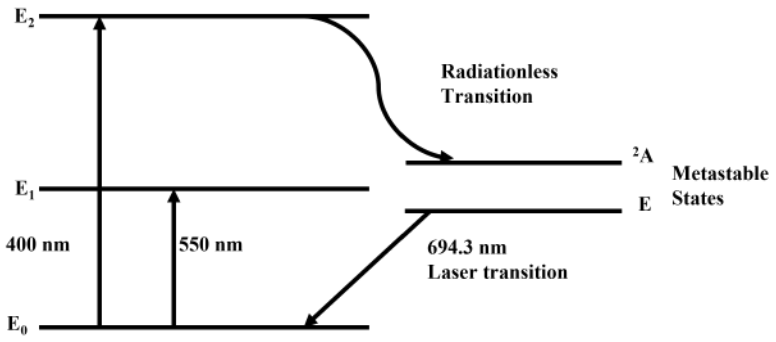

Figure 2.11: Ruby laser electronic transition.

The extended duration of the high laser level permits the excitation of nearly every Cr^{3+} ion in a ruby crystal, and the production of extremely large pulse energy via Q-switching as shown in **Figure 2.12**. The primary applications are high-strength pulse source coherent interferometric radiation, pulse holography, drilling of the fragile material, soldering, welding, and in-range detection [77].

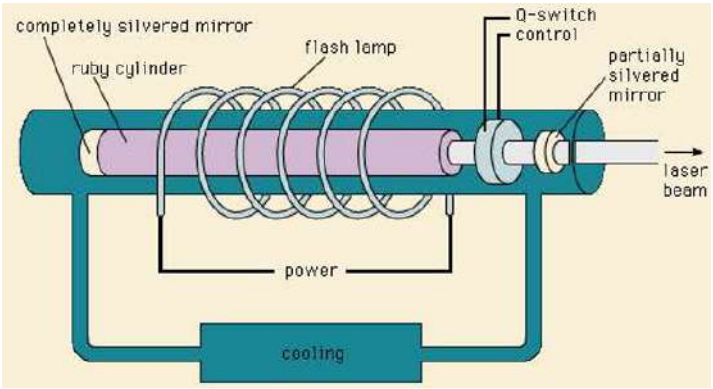

Figure 2.12: Q-switch output pulse switching device for ruby lasers (Image courtesy of [78]).

(II). **Yttrium Aluminium Garnet (YAG) Laser.**

This is a solid-state laser emission device composed of crystalline yttrium and aluminum oxide with a network that serves as a host and is doped with neodymium to produce the species ($Nd : Y_3Al_5O_{12}$), which is a variation of garnet, with a typical wavelength emission of 1064 nm [79]. In 1964 (J.E. Geusic *et al.*) demonstrated the operating mechanism of Nd: YAG in Bell Laboratories for the first time [80].

Nd: YAG lasers are powered by Xe (pulsed) and Kr (CW) discharge lamps. They are among the most widely applied lasers, mainly for industrial purposes. In conventional Q-switched mode, an optical switch is placed into cavity awaiting population inversion of the neodymium ions. The light wave may then flow down the cavity

and depopulate the stimulated laser medium at maximal population inversion as demonstrated in **Figure 2.13**. The Q-switched mode can produce 250-megawatt output and 10 to 25 nanoseconds of pulse length [81].

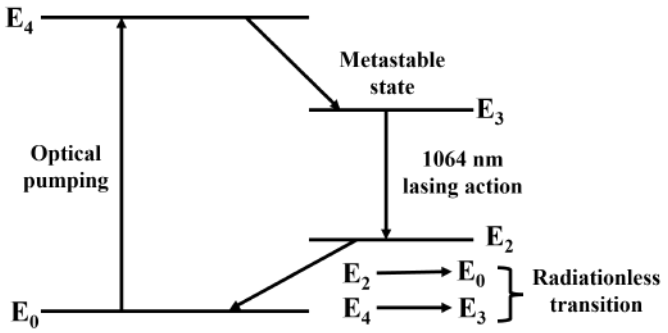

Figure 2.13: Nd: YAG laser quantum transitions

The quantity of neodymium doping concentration in the material depends on its application. Doping is much lower for continuous-wave emissions compared to pulsed ones [82]. The weakly doped CW rods are visually less pigmented and almost white, whereas the highly doped rods are pink-purple. Other neodymium hosts include YLF (1047 and 1053 nm) [83], YVO4 (1064 nm) [84], and glass [85].

The applications of Nd: YAG laser include [61]:

Welding: this may be done in the vicinity of a heat-sensitive area without causing any harm to the material. Nd: YAG is one of the main types of lasers used in welding.

Cutting: hard metals such as stainless steel, carbon steel, and Titanium may be hazardous if not cut correctly. A laser beam is utilized in conjunction with a highly reactive gas, such as oxygen.

Eye surgery: the detached retina is treated with a laser beam. The beam is employed to create a small spot-weld on the retina exactly where it is required.

Figure 2.14 shows an internal structure of the Nd-YAG laser.

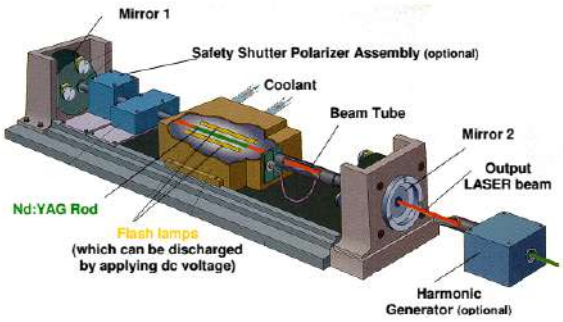

Figure 2.14: An internal structure of the Nd: YAG laser (Image courtesy of [86]).

(III). **Fiber Laser.**

To understand the pumping mechanism, let's consider a 1550 nm fiber laser that we constructed in advanced fiber laser laboratory (CIO Aguascalientes), as shown in **Figure 2.15**. It was pumped using a 980 nm Laser Diode (LD) which was spliced to the Wavelength Division Multiplexer (WDM). The WDM combined the two wavelengths, that is, 980 nm and the 1550 nm (from the coupler). The two wavelengths from the WDM were then channeled to the Erbium-doped Fiber Amplifier (EDFA) which served as the gain medium. In the EDFA, atoms from the ground state were excited by the incoming signal from the LD and jumped to the excited state where they lasted for $\approx 3\mu s$ before losing energy and falling to the metastable state [87]. Atoms lasts for 2∼10 ms at the metastable state before falling to the ground state where they are stimulated by the incoming signal, emitting photon energy (fiber laser). The circulator prevents back reflection inside the fiber cable. A 1550 nm Fiber Bragg Grating (FBG) reflects only a single wavelength (1550 nm in this case) while transmitting the rest. The reflected signal is then transmitted to the 90/10 coupler where it is split into 90 % and 10 %. Part of the signal is analyzed using Optical Spectrum Analyzer (OSA), while the rest is taken back to the WDM to sustain the signal cycle.

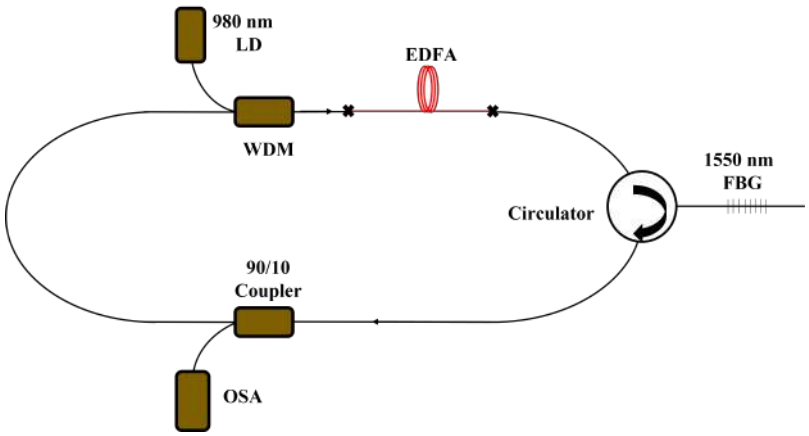

Figure 2.15: Construction of a 1550 nm fiber laser.

To dope an optical fiber with the active gain medium in fiber lasers, rare-earth elements like holmium, thulium, and dysprosium may be utilized [88]. They enhance light without lasing, comparable to doped fiber amplifiers. Fiber-optic lasers are superior to conventional lasers in that they employ an innately flexible medium to transmit the laser beam to the workpiece and concentrate position more easily [89, 90]. For laser cutting, soldering, and cleaning of metals and polymers, this may be vital. Another benefit compared to other laser types is its greater output power. Fiber lasers may have many kilometers of active medium and thus provide extremely large optical gains [91].

Since the fiber cables have a high surface area to volume ratio, they can sustain a continuous output of power levels in kilowatts without overheating. Thermal distortion of the optical channel may be reduced or eliminated by using the fiber's waveguide capabilities, which results in a high-quality optical beam. Due to the ability of the fiber to be twisted and folded, particularly in the case of bigger rod-type devices, fiber lasers are more versatile than equivalent power, gas/solid-state lasers.

Fiber lasers are classified depending on:

Operation mode: there are many distinct kinds of fiber lasers, and each one produces a different sort of light beam. As with "Q-switched", "gain-switched", and "mode-locked" pulsed fiber lasers, high peak powers may be achieved using a predetermined repetition rates. They may also be continuous, which means that they transfer the same quantity of energy.

Mode: the optical fiber's core diameter (the path used by light) is referred to as the mode. Single-mode fiber lasers have a small core (8 to 9 micrometers), while multi-mode fiber lasers have a large core (50 to 100 micrometers). Often, single-mode lasers are more efficient and produce superior beams.

Laser source: fiber lasers differ depending on the substance they are combined with. Examples include ytterbium, thulium, and erbium-doped fiber lasers. Because they generate diverse wavelengths, these lasers are employed in various purposes.

2.2.3 Laser Operational Modes

There are different modes of laser operation. The most essential ones are continuous wave (CW) and pulsed modes.

CW Operation: is the laser-powered constantly and continually producing light, either in a single resonator or in many modes [92]. The peak, lowest and mean powers are almost the same. They do not apply the time and pulse width except when the light is tuned.

Pulsed Operation: is the laser not categorized as a continuous wave, such that optical power emerges at some repeat rate in pulses of a certain period [93]. This includes a broad variety of technologies that address various motives. Some lasers are merely pulsed since they can't be continuously operated. The laser generates no light between the pulses. The period is measured from the beginning of one pulsation to the next. The comparison between CW and pulsed lasers is graphically shown in **Figure 2.16**.

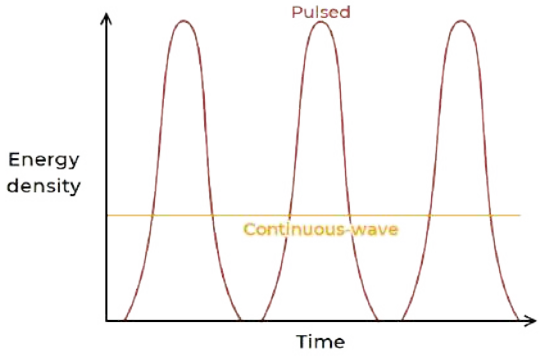

Figure 2.16: A comparison between CW and pulsed operation.

2.3 Laser-Matter Interaction

With sufficient power from the laser, the sample's temperature rises to the melting point because of laser-matter interaction process whereby light energy is transformed to heat energy [94]. The surface is melted and evaporated in form of a plasma plume leaving a cleaned surface.

2.3.1 Thermodynamic Effects

When a material is exposed to laser irradiation, the incoming energy is absorbed, which results to increase in temperature and the development of thermal stress and expansion in the material [95, 96]. It is possible for a material to break or deform if the stress surpasses a specific level. The refractive index, heat capacity, and other

properties of a material may change as it expands. At a depth x, the temperature is measured perpendicular to the surface of the material [97]:

$$\Delta T(x,t) = 2(1-R)\alpha I_0 \frac{t}{\pi\kappa\rho C} iercf \frac{x}{2\sqrt{\kappa t/\rho C}} \tag{2.2}$$

where κ represents thermal conductivity, t is the pulse length, ρ is the density of the material, R denotes reflectivity, I_0 denotes the spatial distribution of intensity, C is the heat capacity of the material, and α denotes the material's absorptivity.

2.3.2 The Mechanism of Melting and Solidification

Laser pulse energy increases, which means that the material will absorb more energy from the pulses and melt when the temperature surpasses its melting point (**Figure 2.17**). The atomic structure of the material may be altered by melting followed by re-solidification, allowing for a transition between crystalline and amorphous states [98].

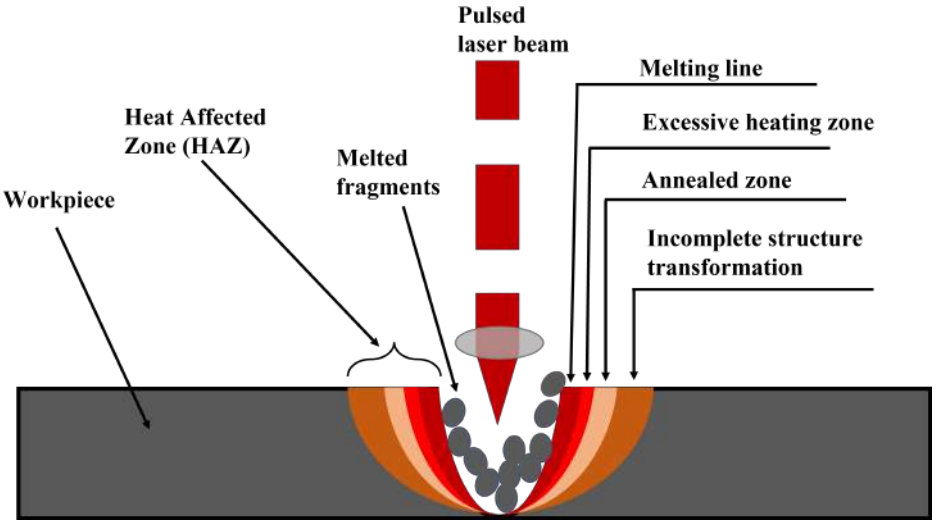

Figure 2.17: The mechanism of melting and solidification.

2.3.3 Gasification and Ionization

Two types of laser-induced gasification exist, i.e surface and bulk [99]. When the temperature rises to the vaporization point, the latent heat of evaporation, and gasification's kinetic energy are all developed. To gasify or ionize the molten material, the laser's intensity must be increased [100]. Particles that have gasified are thrown

to a distance of several microns from the surface. *Knudsen layer* (space populated with ions) is formed between the molten zone and the vapor as illustrated in **Figure 2.18**.

Ionization of the laser energy significantly increases its absorptivity and deposition by the sample. and deposition. The inverse Bremsstrahlung absorption characterizes the absorption of plasma after ionization is complete [101]. The ionized material may undergo a re-crystallization process that alters its structure.

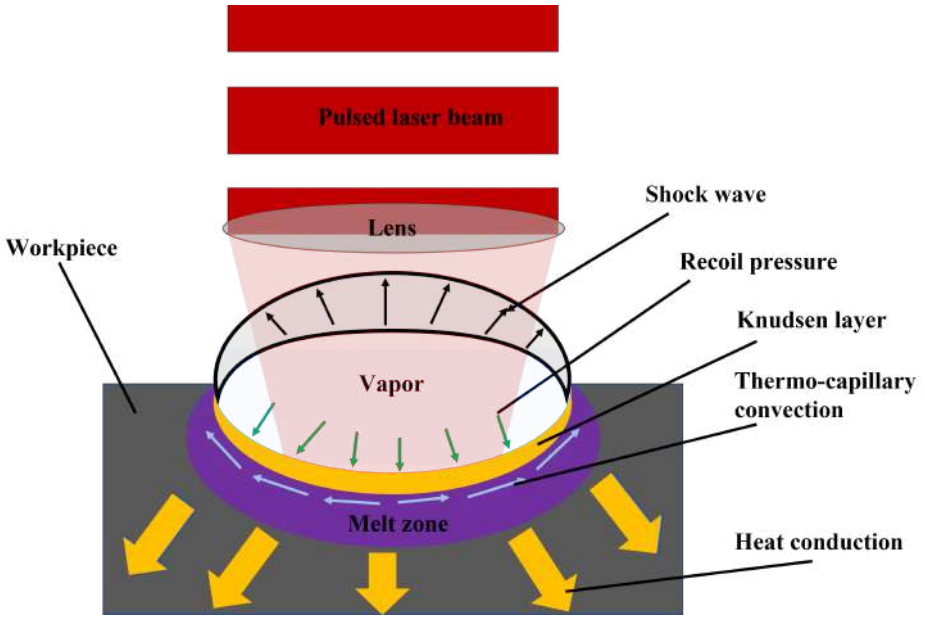

Figure 2.18: Gasification and ionization process.

2.3.4 Explosion of the Phase

Another major thermodynamic phenomenon is phase explosion. The creation and growth of nucleation in the extremely heated liquid, as well as the bursting of the nucleus, are the mechanisms that lead to phase explosions [102]. **Figure 2.19** shows the physical mechanism in action. Thermal conductivity increases fast beyond the boiling point when laser energy is deposited strongly (**Figure 2.19a**); due to the lack of nucleation, however, the boiling doesn't really commence and the liquid becomes very hot (**Figure 2.19b**); Because the absorbed energy disperses to a particular depth into the material's lattice during the disruption, crystals will form (**Figure 2.19c**); The phase explosion occurs this way (**Figure 2.19d**).

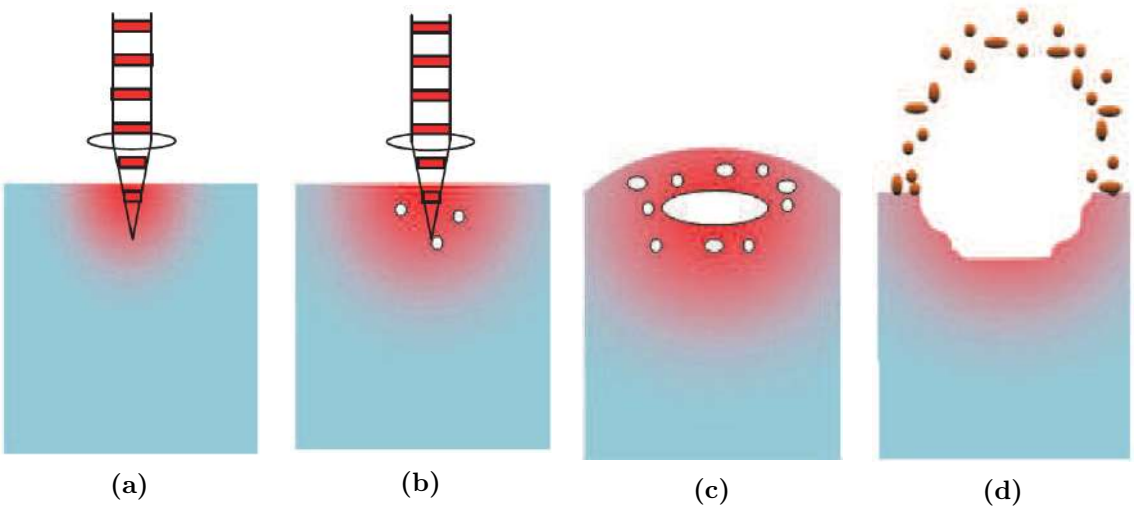

Figure 2.19: The process for the generation of phase explosions.

Phase explosion can only be generated if three conditions are satisfied [103]:

- the critical temperature (Tcr) should be at least $80 - 90\%$ of the incident temperature from the laser pulse for the rapid formation of superheated liquid.
- superheated liquid has a thickness big enough to contain the nuclear, which is typically several tens of microns in thickness.
- the amount of time (t_c) in which the nucleation achieves the critical size (r_c) should be a few hundreds of picoseconds.

Phase explosions need a combination of laser pulses and material parameters. Laser pulses should have a power density greater than the material's threshold. An even higher repetition rate may be used than a single pulse to cause a phase explosion [98].

2.4 Optical Properties of Metals

Laser radiation is an electromagnetic wave and therefore interacts with the matter based on its properties. Since metals are made up of electrons, they absorb kinetic energy from the radiation, setting them into a state of constant vibration. The absorbed energy can either be reflected (depending on the material's reflectivity) or passed on to the lattice structure.

When the laser pulse interacts with the surface of the sample, oscillating electrons develop an electric field and hence the metal becomes polarized. The resultant field

will therefore comprise of the combination between the incident field and the field created due to oscillating electrons. This will eventually determine how the metal will respond to the laser irradiation [104].

Lambert-Beer law states that "the strength of electromagnetic radiation decreases exponentially throughout the absorption process" [105]. This can be given as:

$$I(z) = I_0 \cdot e^{-\alpha \cdot z} \tag{2.3}$$

whereby α is the absorption coefficient, I_0 is the initial intensity, I is the final intensity, and z is the absorption depth.

2.5 Fundamental Parameters for Laser Cleaning

The power density required to elevate the sample temperature to the value required for a phase transition is provided by [106]:

$$I = \frac{E}{\pi f^2 \theta^2 t} \tag{2.4}$$

where f denotes a focal length of the beam, t is the pulse length, E is the pulse energy, θ is the beam's divergence, and I is the power density (fluence).

Additionally, the thermal diffusivity value is essential, which determines the rate of heat dispersion through the material [107]. Temperature increases slowly in materials with a high thermal diffusivity and excellent thermal penetration to the material's surface, in contrast to materials with a low thermal diffusivity, which undergoes a rapid temperature rise and poor thermal penetration. This can be given as:

$$T_s = T_0 + 2I\frac{(1-R)}{\kappa}\left(\frac{Nt}{\pi}\right)^{\frac{1}{2}} \tag{2.5}$$

where T_s and T_0 denotes the final and initial surface temperatures respectively, R denotes reflectivity, N denote the thermal diffusivity, κ denotes the thermal conductivity, t is the pulse length, and I denotes the fluence.

The wavelength is determined by the reflectivity value, which is one of the most essential features. A considerable laser fluence is required to ablate the surface since most metals reflect some percentage of the incident beam [108].

2.6 Laser Machining

Laser processing, such as employing laser energy to heat metals, results in light absorption and reflection on the workpiece [109]. There are several factors that influence metals' ability to absorb light: wavelength, type of material, incidence angle, and surface quality.

As observed in **Figure 2.20**, aluminium for instance has the maximum absorption at a wavelength of about 0.1 μm and the minimum at 20 μm. Stainless steel is only absorbed from a wavelength of about 1.064 μm, and the absorption significantly drops with increasing wavelength. Each analyzed metal exhibits a specific trend, with similarity associated with a decreasing absorption with increase in wavelength. With respect to the analyzed lasers, the wavelength of 10.6 μm (which corresponds to CO_2 laser) is the least absorbed by most of the observed metals.

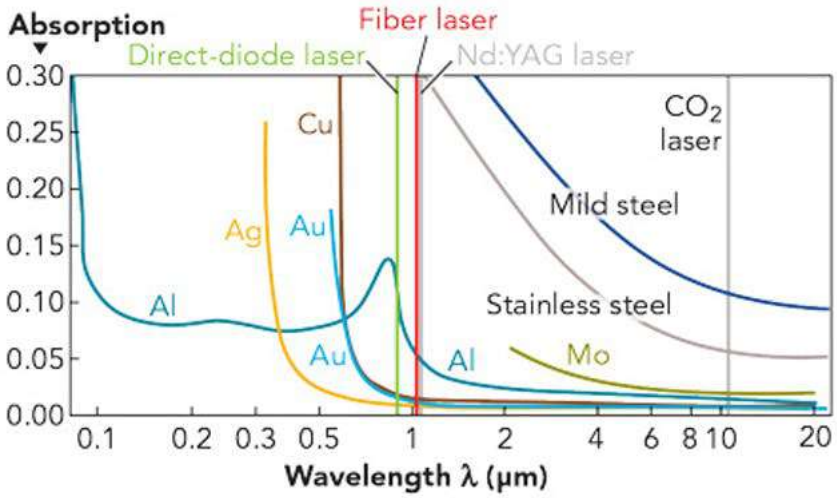

Figure 2.20: Absorptivity of laser energy versus wavelength for various metallic samples (Image courtesy of [109]).

Chapter 3

Methodology

3.1 Introduction

In our experimental process, we applied both CO_2 and fiber lasers. Each of the lasers was used to clean the same type of samples under ambient environmental conditions. The application of two lasers was to identify one with the best cleaning parameters based on the analyzed results. The samples to be cleaned were selected based on the level of corrosion, varying surface structure and industrial application. Two samples were selected; high carbon steel and grey cast iron. The corrosion percentages of both carbon steel and grey cast iron were approximated to be 30% and 47% respectively.

High carbon steel is among the most currently applied metals for industrial purposes especially in the manufacture of wrenches, knives, railway wheels, cold chisels, drill bits, springs, shear blades, among others. Grey cast iron on the other hand is widely applied in the manufacture of gearbox cases, engine cylinder box, cookware, flywheels, manifolds, among others. The fact that most of the devices produced from both metals operate in the outdoor and in harsh environmental conditions, the risk of corrosion is very high.

Different characterization techniques were applied to analyze the experimental results of both cleaned and uncleaned samples:

1. Raman spectroscopy was used to identify the type of iron oxide (corrosion) that could be present in the samples. This was achieved by identifying the bands of each sample and comparing them with the database of the respective metal oxides found in literature. In addition, the carbon bands related to the

carbon content of each sample were also analyzed using Raman spectroscopy.

2. The optical microscopy was used to analyze the surface topography after the cleaning process. Using this information, the roughness of each sample was found.

3. Information obtained from the Scanning Electron Microscope (SEM) helped us to analyze the presence of surface fractures, determine the crystalline structures, and identify the surface microstructures of the samples.

4. The information obtained using Energy Dispersive Spectroscopy (EDS) not only helped us identify the chemical elements present in the samples but also their relative abundance in terms of percentage.

Lastly, a mathematical simulation of carbon steel and cast iron was developed using Finite Element Analysis (FEA) technique in MatLab and Ansys Workbench. The FEA technique was adopted because it provides more information about the thermodynamic processes taking place in the sample during the laser cleaning, some of which may be overlooked in the experimental approach. The meticulous analysis of FEA results also helped us make necessary modifications of the experimental process.

It should also be noted that, the experimental process is presented before the simulation so as to take into account both the negative and positive effects drawn from the experimental process. The simulation is mostly focused on visualizing and explaining some of the experimental outcomes that could otherwise be impossible to understand.

3.2 Properties of Carbon Steel

Carbon steel AISI 1095 (shown in **Figure 3.1**) is one of the most useful grades of steel due to its high hardness relative to others [110]. Its carbon content ranges between 0.60% to 1.00% which contributes greatly to its hardness and abrasion resistance.

Figure 3.1: Uncorroded hot-rolled carbon steel plates (image courtesy of [110]).

The main properties of carbon steel AISI 1095 which have been widely discussed in [110–113] are summarised in **Tables 3.1**, **3.2**, and **3.3**.

3.2.1 Chemical Properties

Carbon steel AISI 1095 is an alloy composed of various elements with different percentage weight. These are outlined in **Table 3.1**.

Table 3.1: Chemical composition of carbon steel AISI 1095.

Element	**Fe**	**C**	**Mn**	**S**	**P**
Wt %	$98.38 - 98.8$	$0.90 - 1.03$	$0.30 - 0.50$	≤ 0.05	≤ 0.04

3.2.2 Physical Properties

These are properties that can be measured or determined experimentally. AISI 1095 carbon steel has a number of such properties as given in **Table 3.2**

Table 3.2: Physical properties of carbon steel AISI 1095.

Properties	**Metric**	**Imperial**
Density, ρ	$7.85\ g/cm^3$	$0.284\ lb/in^3$
Melting point	$1515\ ^oC$	$2760\ ^oF$

3.2.3 Thermal Properties

These properties are very useful during heat application on carbon steel AISI 1095. As a matter of fact, they played a major role in both simulation and experimental

process of the present work. They are outlined in **Table 3.3**.

Table 3.3: Thermal properties of carbon steel AISI 1095.

Properties	**Metric**	**Imperial**
Thermal expansivity (@ 0.00-100 ^0C/32-212 ^0F)	11.00 $\mu m/m^0C$	6.11 $\mu in/in^0F$
Thermal conductivity	49.8 W/mK	346 BTU $in/hr.ft^2.^0F$

3.2.4 Effects of Corrosion on Carbon Steel

When exposed to harsh environmental conditions, degradation of carbon steel takes place either immediately or gradually depending on prevailing conditions. **Figure 3.2** shows a corroded carbon steel plate after being exposed to the ambient environment in Aguascalientes state of Mexico for a period of three months.

Figure 3.2: Corroded carbon steel plate.

There was a remarkable loss in the physical structure of the material during corrosion process. For instance, the density reduced from 7.85 to 7.78 g/cm^3. The shiny, metallic surface was also replaced with a dull, dark-brown surface which significantly affected the quality of the original carbon steel sample.

3.3 Properties of Grey Cast Iron

Grey cast iron ASTM A159 (an example is the brake disk shown in **Figure 3.3**) is distinctively identified by the presence of graphite flakes in its structure which also accounts for the existence of micro-pittings as viewed from the surface upon magnification. Some of the properties of uncorroded grey cast iron are given in

Tables 3.4, 3.5, 3.6, and **3.7**. The given data is courtesy of "American Society for Testing and Materials (ASTM)" [114] and is with respect to room temperature.

Figure 3.3: Uncorroded brake disk.

3.3.1 Chemical Properties

Grey cast iron ASTM A159 is an alloy composed of various elements that are combined in different percentage weight as provided in **Table 3.4**

Table 3.4: Chemical composition of cast iron ASTM A159.

Element	**C**	**Mn**	**P**	**Si**	**S**
Wt %	$3.1 - 3.4$	$0.6 - 0.9$	0.15	$1.9 - 2.3$	0.15

3.3.2 Thermal Properties

Table 3.5: Thermal properties of cast iron ASTM A159.

Properties	**Temperature**	**Quantity**
The coefficient of thermal expansion	300 K	$1.1 \times 10^{-5} - 1.5 \times 10^{-5} K^{-1}$
Specific heat capacity	300 K	$460 J/(kg.K)$
Thermal conductivity	300 K	$20 - 80 W/(m.K)$

3.3.3 Mechanical Properties

Table 3.6: Mechanical properties of grey cast iron ASTM A159.

Properties	Temperature	Quantity
Elastic modulus	300 K	92.4 GPa
Hardness, Brinell	300 K	$187 - 241$ MPa
Poisson's ratio	300 K	0.21
Shear modulus	300 K	41 GPa

3.3.4 Physical Properties

Table 3.7: Physical properties of grey cast iron ASTM A159

Properties	Temperature	Quantity
Density, ρ	300 K	$7.15 g/cm^3$
Melting point		$1127 - 1204^0 C$

3.3.5 Effects of Corrosion on Grey Cast Iron

Figure 3.4 shows the corroded brake disk after an exposure to the ambient environment in Aguascalientes state of Mexico for a period of three months. The estimated corrosion percentage was 65 % after a loss in mass of about 10 %. The corroded brake disk significantly compromised the original quality as a result of the loss of shiny, metallic appearance as well as reduction in hardness from approximately 235 to 210 MPa.

Figure 3.4: Corroded brake disk.

3.4 Experimental Methodology

To perform the experiments, a 20 W fiber laser with 1070 nm wavelength and 120 ns pulse duration as well as a 30 W $CO2$ laser with a pulse duration of 2000 ns, and a wavelength of 10600 (nm) were also used.

3.4.1 Focusing the Laser Beam

The laser beam was focused on the sample using a galvo-head and an f-theta lens. The main function of the galvo-mirrors was to facilitate the motion of the beam in a raster format (progressive coverage of a scan area, one motion at a time). On the other hand, the f-theta lens ensured that the beam was focused in a planar form.

3.4.1.1 The Working Principle of F-theta Lens

F-theta lenses are meticulously designed through a combination of multiple spherical or aspherical lenses to focus the laser beam on a plane surface with uniform optical distribution in terms of intensity and resolution [115]. This limits the margin error experienced in laser machining. Additionally, no technical software is needed to enhance beam distribution on the sample. The product between the angle, θ, at which the incident beam is deflected from the galvo-mirrors and the effective lens's focal length, f, is the principal determining factor of the size of the image which is given as [116];

$$h_i = f \cdot \theta \tag{3.1}$$

It should be noted that equation 3.1 is especially important to offer a certain amount of distortion on the focused image (Δh_i) which helps to maintain a constant scan speed on the sample.

Figure 3.5: The working principle of an f-theta lens.

In our case, the fiber laser had an f-theta lens whose focal length was 290 mm and a 1070 nm wavelength, whereas CO_2 laser had 150 mm focal length and a 10600 nm wavelength. The spot sizes were 50 μm and 150 μm FWHM for the fiber and the CO_2 lasers respectively.

3.4.1.2 The Working Principle of the Galvanometer Scanning Head

The galvo-scanning head was responsible for adjusting the position of the beam on the surface of the sample. Moreover, it also helped to ensure beam motion in a raster format. It is made of X and Y tilting mirrors which are meticulously positioned to enhance a maximum beam reflection.

The beam expander directs an incident beam from the laser to the galvo-mirrors whose position/angle is manually manipulated using designated computer software. Both mirrors may be positioned to divert the laser beam in x and y directions. Given in **Figure 3.6** is an illustration of how the galvo-mirrors are positioned as well as their working principle.

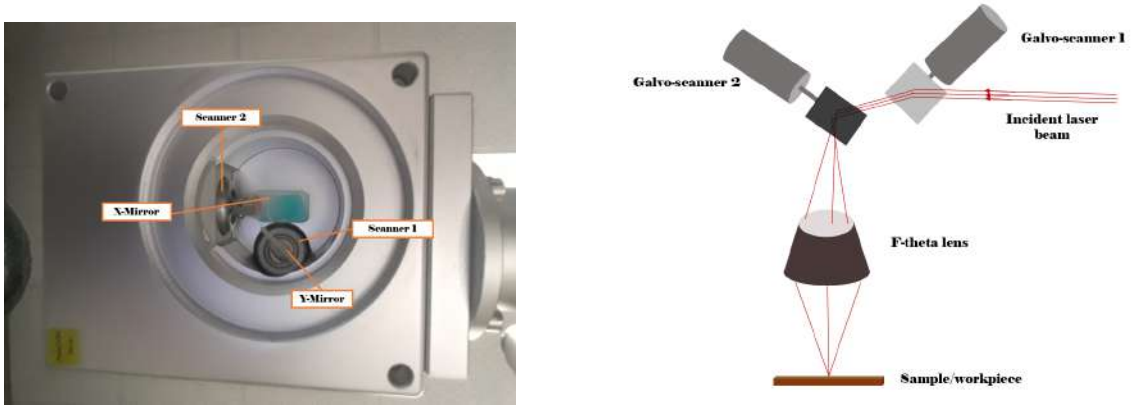

(a) **(b)**

Figure 3.6: Galvanometer scanning head (a) X and Y mirror arrangement, and (b) working mechanism.

The experimental setup used in the cleaning process is shown in **Figure 3.7**.

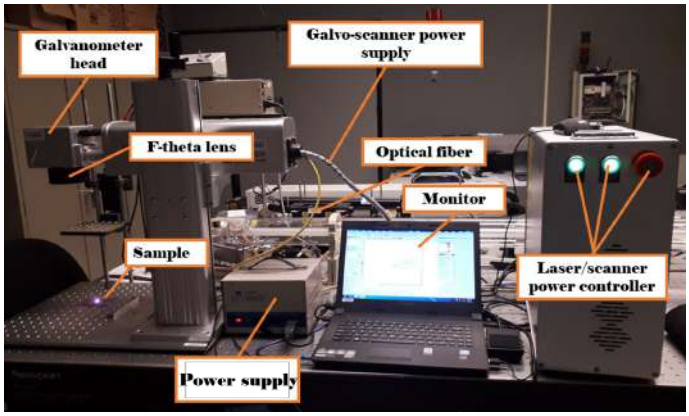

(a)

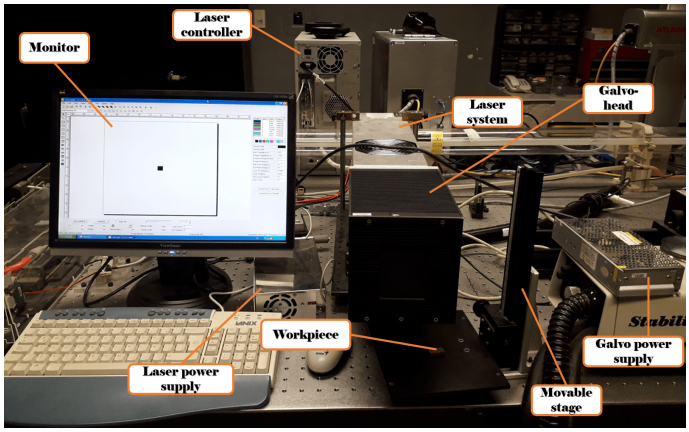

(b)

Figure 3.7: The set-up used for experimental laser cleaning (a) using the fiber laser, and (b) using CO_2 laser.

Three samples each measuring 10 mm by 10 mm were cut from both carbon steel and cast iron. Two of the samples (for each metal) were cleaned using the Fiber

laser and CO_2 laser respectively, while one was left uncleaned. Dry laser cleaning (DLC) technique was adopted in this experiment.

The samples were placed on the working bench at a focal length equivalent to that of the F-theta lens. This was done to ensure maximum dissipation of the beam intensity on the sample during the cleaning process. To adjust the focus, a supplementary sample of the same thickness was used with random laser parameters. Two scanning patterns (shown in **Figure 3.8**) were used.

(a) **(b)**

Figure 3.8: Laser scanning patterns used in the cleaning of carbon steel and cast iron (a) continuous, and (b) lineal.

The laser pattern in **Figure 3.8a** depicts that, the beam scans the surface of the sample from right-to-left, then left-to-right along the same path, while the pattern in **Figure 3.8b** shows that the laser beam scans from left to right and then 'jumps' back to the origin before making another scan. Both patterns rendered a distinctive effect on the cleaned samples.

3.5 Characterization of the Samples

The element composition and surface analyses were conducted using a Scanning Electron Microscope (SEM JEOL JSM-5900LV) equipped with Energy Dispersive X-ray Spectroscopy (EDS). Different spots were randomly selected and analyzed. Moreover, the laser spot size was also measured.

The roughness of the samples was analyzed using a Keyence digital microscope which utilizes a digital camera to magnify the sample up to 7000× with a 4K resolution. A line profile was drawn diagonally across the image of each sample to obtain an average roughness. The microscope was also used for microstructural analysis of the laser cleaned areas on the surface of each sample.

Raman spectra of the samples were measured using a micro-Raman with iHR320

spectrometer, an excitation laser at 633 nm (with a spot-size of about 0.8 mm) in a backscattering geometry onto the sample, and a microscope with a 40X objective lens. The equipment was calibrated using a silicon wafers 520 cm^{-1} Raman line. Measurements were taken at numerous locations. The output current from the laser was moderated using a filter to prevent damage to the surface structure which could affect the resultant Raman bands.

3.6 Mathematical Simulation to Demonstrate Heat Distribution During Cleaning of Carbon Steel and Cast Iron

The first mathematical simulation was modeled using *pdepe* solver in MatLab (2021 a) based on a two-temperature model (TTM). This methodology has been previously applied in the ablation modeling of aluminum[117], copper[118] and gold [119].

The TTM is given by two fundamental one-dimensional partial differential equations which fully describe heat flow from the source (laser) to the sample over a given period of time. This model was first proposed by Russian scientists, Kapeliovich and Anisimov in 1974 [120]. It is given by:

$$C_e \frac{\partial T_e}{\partial t} = \frac{\partial}{\partial z}\left(\kappa_e \frac{\partial T_e}{\partial z}\right) - g(T_e - T_l) + S(z,t) \tag{3.2}$$

$$C_l \frac{\partial T_l}{\partial t} = g(T_e - T_l) \tag{3.3}$$

$$S(z,t) = \sqrt{\frac{\beta}{\pi}} \frac{(1-R)F\alpha}{\tau} \exp\left[-\alpha z - \beta\left(\frac{t-\tau}{\tau}\right)^2\right] \tag{3.4}$$

whereby C_e and C_l are electrons and lattice-specific heat capacities of the sample respectively, T_e is the electron temperature, κ_e represents heat conductivity of electrons, z is the directionality vector of the laser beam propagation, T_l is the lattice temperature, g is the coupling factor of surface electrons and the lattice structure, S represents laser origin term, $\beta = 4\ln 2$, R is the reflectivity, F is the fluence, τ is the pulse width, α is the absorption coefficient and t is the laser pulse duration.

Temperature dependence of electronic heat capacity C_e is very crucial in this model as it helps us to understand how the sample interacts with laser radiation. Since

this research involves metallic samples, C_e can be given as [121]:

$$C_e = \frac{\pi^2 n_e}{2}\left(\frac{k_B T_e}{E_F}\right) k_B \equiv \gamma T_F \tag{3.5}$$

whereby n_e is the electron concentration, κ_B is the Boltzmann constant while E_F and T_F are Fermi energy and temperature respectively. The MatLab simulation was implemented as shown in **Figure 3.9**.

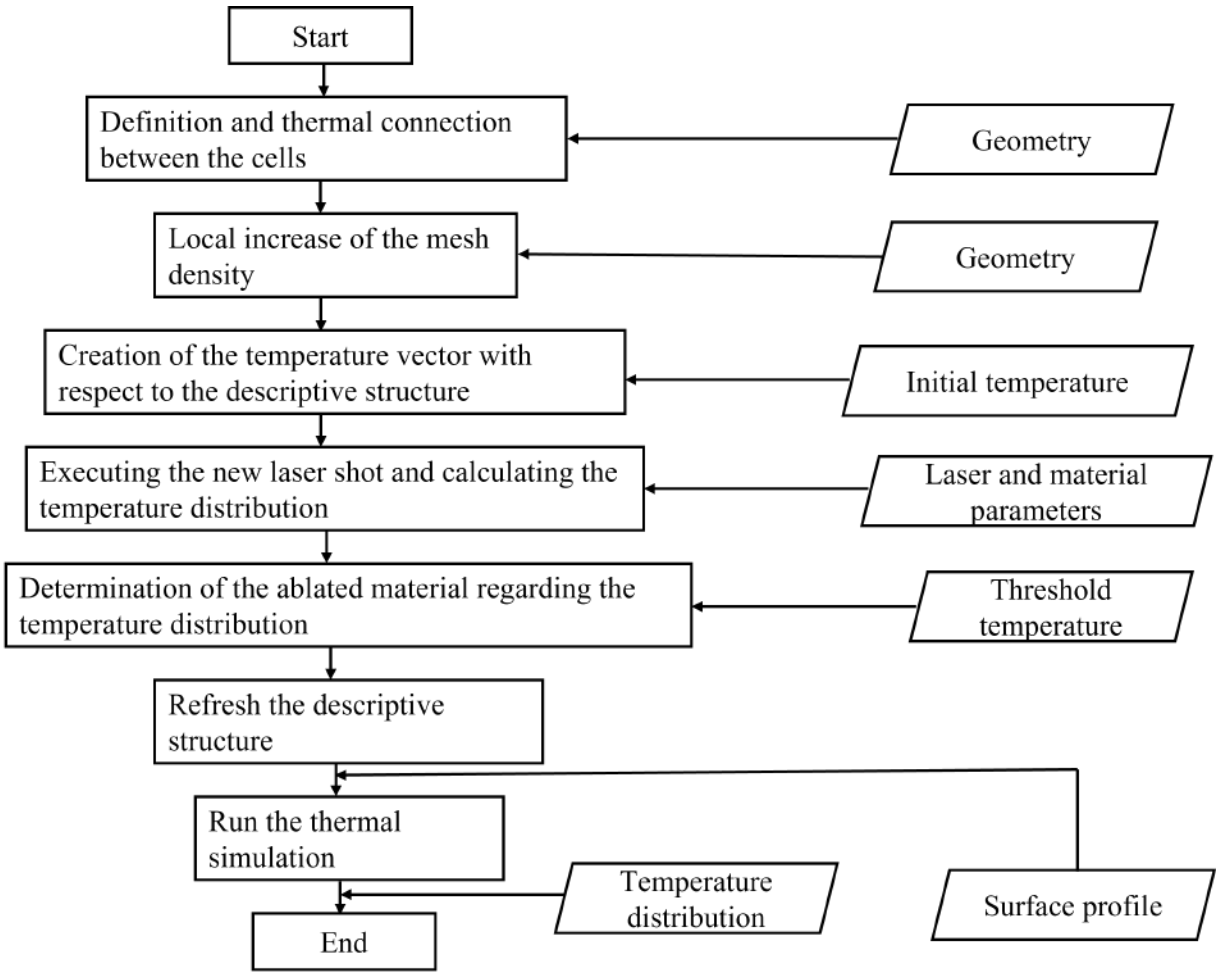

Figure 3.9: Simulation process implemented in MatLab.

The second simulation was implemented using transient thermal in ANSYS workbench (2020 R2). This enabled us to understand how the laser beam interacts with different surface micro-structures. Carbon steel for instance, has a pearlitic microstructure [122], while grey cast iron has graphitic micro-structure [123]. The model was implemented as shown in **Figure 3.10**.

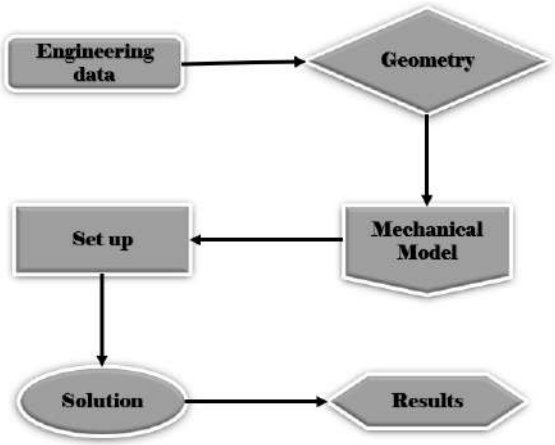

Figure 3.10: Simulation process implemented in ANSYS workbench.

The engineering data for both samples were obtained within ANSYS software. The geometry was designed using DesignModeler and imported into Mechanical Model (MM) where the rest of simulation was performed. A moving laser source was simulated and heat distribution on both surfaces was observed, which was later compared to the experimental results. In addition, surface ablation was also simulated.

The laser parameters used in the simulation process are shown in **Table 3.8**.

Table 3.8: Laser parameters used in the simulation process [124, 125]

Laser Parameter	**Value (CO_2 Laser)**	**Value (Fiber Laser)**
Wavelength, λ (μm)	10.6	1.07
Frequency, f (kHz)	2, 3, 4, 5	20, 40, 60, 80
Spot Diameter, D (μm)	150	50
Pulse Duration, τ (ns)	2000	120

The simulation parameters for each sample are given in **Table 3.9**.

Table 3.9: Material parameters used in the simulation process [126–129]

Material Parameter	**Value (Grey cast iron)**	**Value (Carbon steel)**
Heat capacity of electrons, γ $(Jm^{-3}K^{-2})$	804.7	705.4
Reflectivity, R	0.53	0.54
Lattice heat capacity, $C_l \times 10^6$ $(Jm^{-3}K^{-1})$	7.401	6.105
Thermal conductivity, κ $(Wm^{-1}K^{-1})$	56	36
Electron-lattice coupling, G $\times 10^6$ $(Wm^{-3}K^{-1})$	137	150
Absorptivity, α $(\lambda = 1070$ nm), m^{-1}	2×10^8	7.1×10^7
Absorptivity, α $(\lambda = 10600$ nm), m^{-1}	2×10^7	7.1×10^6

Chapter 4

Results Analysis and Discussion

4.1 Introduction

In this chapter, we shall analyze both experimental and simulation results and the comparison between them. Cleaned samples from both fiber and CO_2 lasers will be presented. An in-depth analysis of the samples cleaned using the fiber laser will also be given by considering Raman analysis, SEM analysis, EDS analysis, and optical microscopy. The samples discussed under fiber laser will be presented with subscript f while those under CO_2 with subscript c.

The Raman was used to analyze the type of oxides present on both cleaned and uncleaned samples by observing their respective positions of the peaks. Furthermore, the presence of carbon bands was also analyzed using this technique. The SEM was used to analyze the surface topography of both the cleaned and uncleaned samples to identify the effects caused by the laser pulses during cleaning process as well as the micro-cracks generated by the corrosion process.

The EDS technique was used to analyze the quantity of elements present in both cleaned and uncleaned samples in terms of percentage. Much consideration was placed upon the quantity of oxide composition on the samples to ascertain efficiency of the cleaning process. The optical microscopy was necessary to analyze the roughness of the samples as well as determine the efficiency of the cleaning process. The importance of optical images was to give the physical appearance of the samples but in a magnified state so as to identify whether some traces of corrosion remained on the surface after the cleaning process.

The simulation results helped us analyze some of the thermodynamic processes

taking place inside the samples that could not be explained experimentally. However, it should be noted that in this case, the experimental results will be presented before the simulation results because some of the ideas in the simulation were drawn from the results obtained experimentally. A perfect example of this is the case where the optical images revealed some corrosion in the micro-pittings (tiny holes on the surface) of grey cast iron. Upon simulation, it was possible to explain the reason behind such results and provide a suggestion for future improvements. All the parameters used in the simulation corresponds to the laser parameters used in the experimental process as well as the sample parameters (grey cast iron and carbon steel) drawn from literature.

4.2 Experimental Results

This section provides experimental results obtained after cleaning carbon steel and grey cast iron. Characterization of the samples that were cleaned using the fiber laser are also discussed.

4.2.1 Carbon (IV) Oxide Laser

Table 4.1 shows some of the parameters used in the cleaning of carbon steel samples using carbon (IV) oxide laser.

Table 4.1: Experimental CO_2 laser parameters used for the cleaning of carbon steel samples.

Sample	S_{c2}	S_{C3}
Scan Speed (mm/s)	500	1000
Hatch Spacing (μm)	50	30
Number of Passes	10	20
Power (%)	50	90
Frequency (kHz)	2.5	4.0
Cleaned Area (mm^2)	100	100
Cleaning Time (s)	100	82

Figure 4.1 shows the physical appearance of the carbon steel samples after the cleaning process using carbon (IV) oxide laser. Sample S_{c1} was left uncleaned. We

observed that despite the variation in different parameters, the surfaces of samples S_{c2} and S_{c3} were left oxidized with very little ablation. This can be attributed to less absorptivity of the incident laser beam.

(a) **(b)** **(c)**

Figure 4.1: Physical appearance of carbon steel samples (a) S_{c1}, (b) S_{c2}, and (c) S_{c3}.

4.2.2 Fiber Laser

Table 4.2 shows various parameters used in the cleaning of carbon steel samples using the fiber laser. We used different combination of laser parameters on various samples and came up with the given parameters as they provide a better scope of comparison. Sample S_{f1} was uncleaned hence not captured in **Table 4.2**. From our analysis, sample S_{f3} had the best cleaning parameters both in terms of physical appearance, the average power and the average cleaning time. The time spent in the cleaning process is very vital since it directly affects the economical aspect of our research work. Additionally, the average power used on sample S_{f3} was 50% which from the analysis done (shown in **Figure 4.2**) represents 5.1 W, which also contributes to the economic aspect of this research.

Table 4.2: Experimental fiber laser parameters used for the cleaning of carbon steel samples.

Sample	S_{f2}	S_{f3}
Scan Speed (mm/s)	1900	1000
Hatch Spacing (μm)	50	30
Number of Passes	30	15
Power (%)	90	50
Frequency (kHz)	50	20
Cleaned Area (mm^2)	100	100
Cleaning Time (s)	80	50

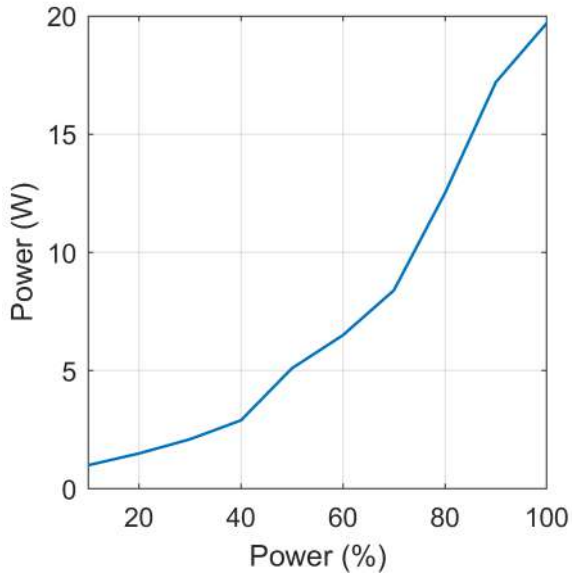

Figure 4.2: Variation between average powers in Watts and percentage of the fiber laser used in experimental process.

Figure 4.3 shows the physical appearance of the three carbon steel samples in both the cleaned and the uncleaned state. The images were taken using a Samsung J4 phone camera. Sample S_{f1} (**Figure 4.3a**) shows high amount of rust due to oxidation. The level of surface melting on Sample S_{f2} (**Figure 4.3b**) is significantly high as compared to that of sample S_{f3} (**Figure 4.3c**) after the cleaning process. A more detailed analysis of the amount of oxide present on each sample as well as roughness will be discussed in the later sections.

(a) **(b)** **(c)**

Figure 4.3: Physical appearance of carbon steel samples (a) S_{f1}, (b) S_{f2}, and (c) S_{f3}.

Table 4.3 shows the fiber laser cleaning parameters for grey cast iron. From our analysis, sample R_{f2} was the less cleaned while R_{f3} was the most cleaned.

Table 4.3: Experimental fiber laser parameters used for the cleaning of cast iron samples.

Sample	R_{f2}	R_{f3}
Scan Speed (mm/s)	1000	750
Hatch Spacing (μm)	50	30
Number of Passes	15	10
Power (%)	70	50
Frequency (kHz)	40	20
Cleaned Area (mm^2)	100	100
Cleaning Time (s)	65	40

Figure 4.4 shows the physical appearance of the grey cast iron samples in both cleaned and uncleaned states. The uncleaned sample R_{f1} (**Figure 4.4a**) shows a high amount of rust due to oxidation by the ambient atmosphere. Some black deposits can be observed on the surface of a sample R_{f2} (**Figure 4.4b**), an indication of oxidation resulting from laser pulses during the cleaning process. Sample R_{f3} (**Figure 4.4c**) shows very tiny black deposits which can be barely observed by a bare eye.

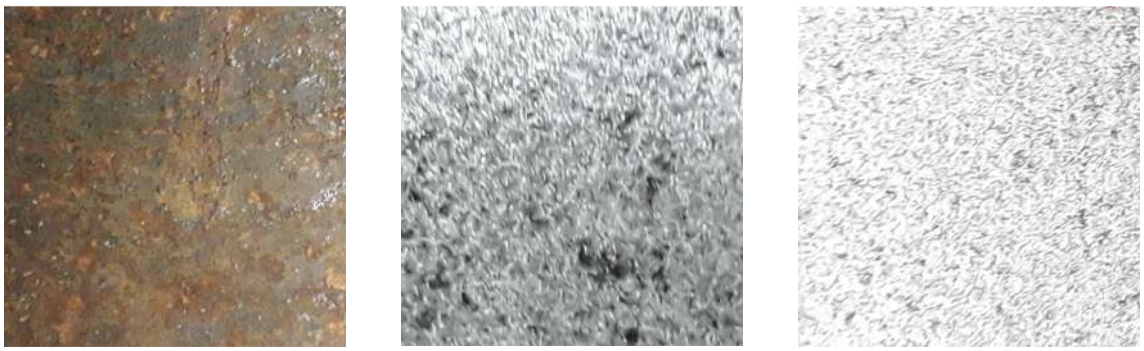

(a) **(b)** **(c)**

Figure 4.4: Physical appearance of grey cast iron samples (a) R_{f1}, (b) R_{f2}, and (c) R_{f3}.

4.2.3 Surface Morphology and Composition

Surface morphology "is a subset of analytical imaging, which is an advanced form of high spatial resolution imaging that uses sophisticated microscopes to produce images of products, samples and objects that cannot be seen with the naked eye" [130]. In our case, we applied Scanning Electron Microscope, and Digital Optical Microscope to analyze the surface effects caused by corrosion as well as the laser pulse during the cleaning process. Composition of the surface compounds was analyzed

using Raman spectrum to determine the various types of oxides present on the samples.

4.2.3.1 Optical Microscopy

In this work, we used Keyence Digital Microscope VHX-7000 (shown in **Figure 4.5**) to analyze the effects of laser cleaning on the samples as well as the average roughness of the surface. The microscope has a magnification of up to 7000× with a high image resolution of 4K quality (3840 × 2160 pixels).

Figure 4.5: Digital optical microscope in use [131]

Figure 4.6 gives the optical image of the less cleaned sample of carbon steel (S_{f2}). Oxidation caused by the laser pulses during the cleaning process can be seen as evidenced by the dark-brownish deposits on the sample's surface. This sample's average surface roughness was determined to be 20 μm.

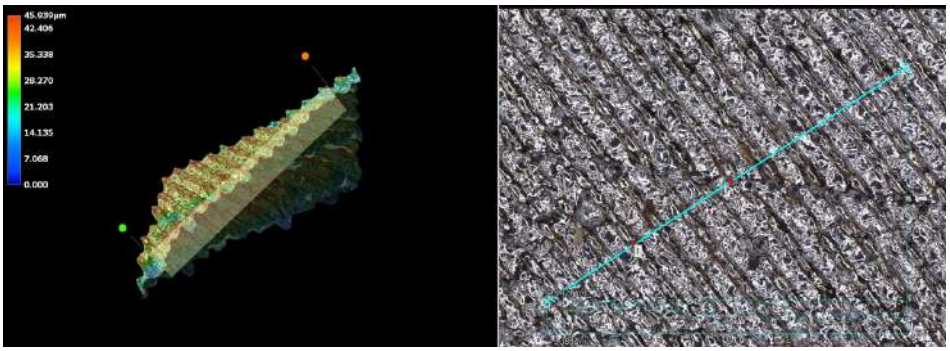

Figure 4.6: Optical analysis of the carbon steel sample S_{f2}

Given in **Figure 4.7** is the optical analysis of the most cleaned carbon steel sample (S_{f3}). In this case, less dark-brownish patches resulting from oxidation due to laser pulses can be observed on the surface in comparison to the sample S_{f2} analyzed

before. In addition, the damage caused by the laser on the sample's surface is less defined. The average surface roughness of this sample was found to be about 6 μm.

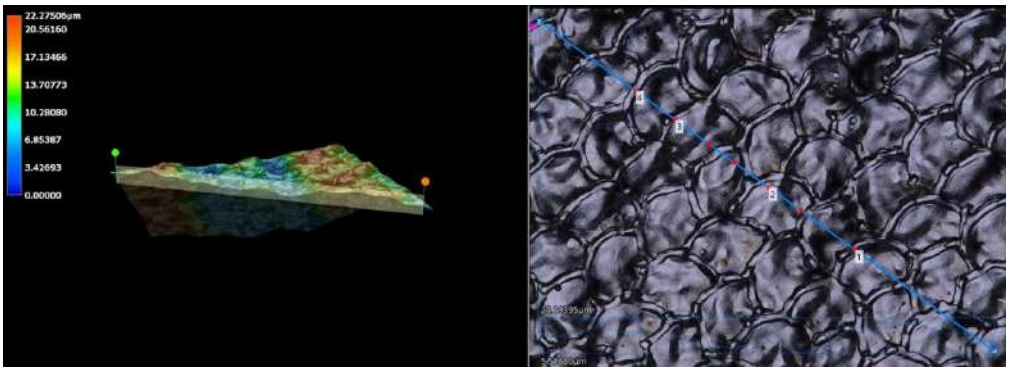

Figure 4.7: Optical analysis of the carbon steel sample S_{f3}

Shown in **Figure 4.8** is the optical analysis of the uncleaned grey cast iron sample (R_{f1}). Surface damage resulting from oxidation due to ambient atmospheric conditions can be vividly discerned, thanks to the high image resolution of the digital microscope. The average surface roughness was found to be about 76 μm.

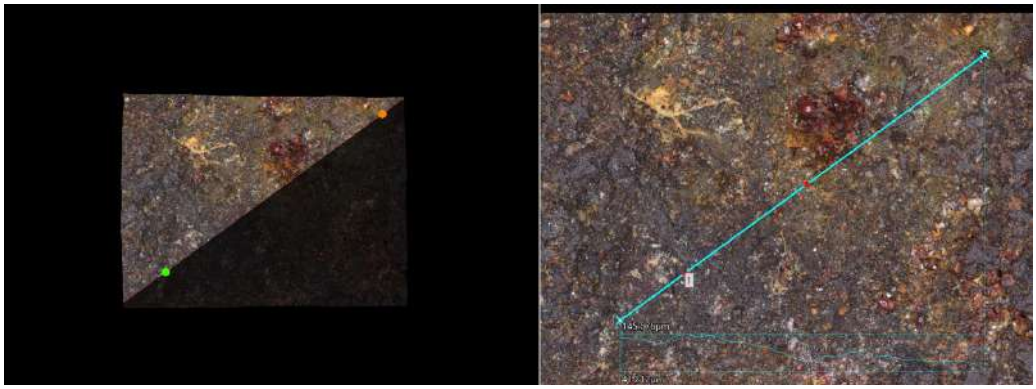

Figure 4.8: Optical analysis of the uncleaned grey cast iron sample R_{f1}

Given in **Figure 4.9** is the optical analysis of the less cleaned sample (R_{f2}) of the grey cast iron. In this instance, we found corrosion inside micro-pittings (tiny holes on the surface) that could not be ablated during the cleaning procedure. This can be attributed to the graphitic microstructure of grey cast iron [132]. In addition, dark patches of laser-induced oxidation can also be vividly observed. The average surface roughness of sample R_{f2} was about 64 μm.

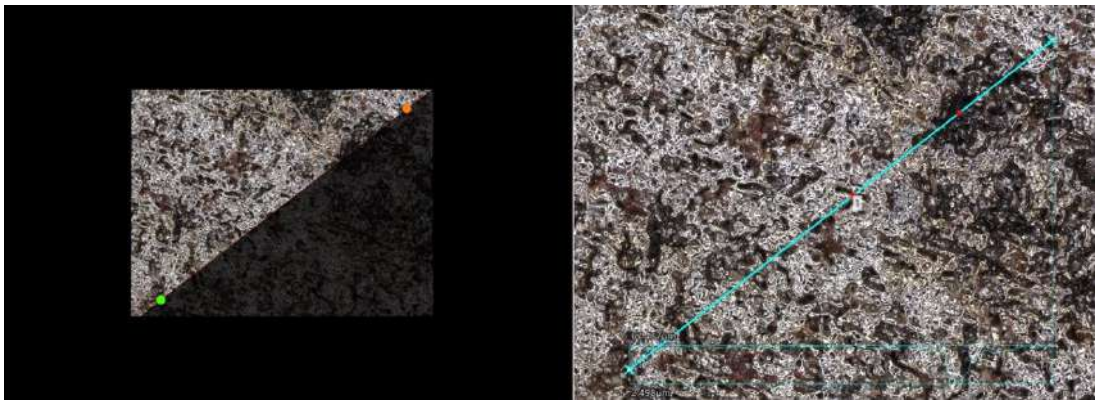

Figure 4.9: Optical analysis of the less cleaned grey cast iron sample R_{f2}

The optical analysis of the most cleaned grey cast iron sample R_{f3} is given in **Figure 4.10**. Similar to sample R_{f2}, we found some corrosion inside the micro-pittings. However, less oxidation resulting from laser pulses was observed on sample R_{f3}. In addition, the less average surface roughness of about 31 μm was observed.

Figure 4.10: Optical analysis of the most cleaned grey cast iron sample R_{f3}

4.2.3.2 Scanning Electron Microscopy (SEM)

In this work, SEM analysis of both cleaned and uncleaned samples of carbon steel and grey cast iron will be presented. The analysis was done using JEOL JSM-5900LV at different spots to observe the effects of corrosion on the surface topography of the uncleaned samples. In addition, the effects caused by laser pulses during the cleaning process were also observed as well as the spot size.

The images of Scanning Electron Microscope of carbon steel samples are shown in **Figure 4.11**. Large crystal deposits of up to 1.5 μm were observed on the surface of the uncleaned sample (**Figure 4.11a**), with cracks of up to 2 μm wide. No crystal deposits were observed on the cleaned samples. However, some tiny cracks of about

100 nm were observed on the surface of the less cleaned sample (**Figure 4.11b**). The most cleaned sample (**Figure 4.11c**) had neither crystal deposits nor cracks.

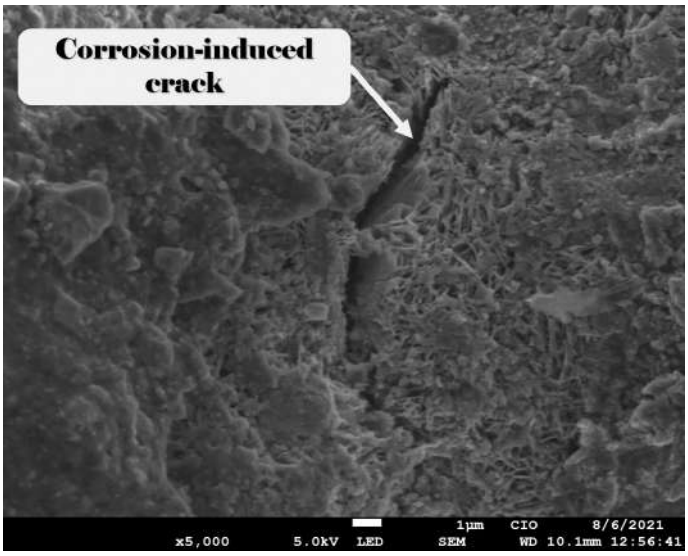

(a)

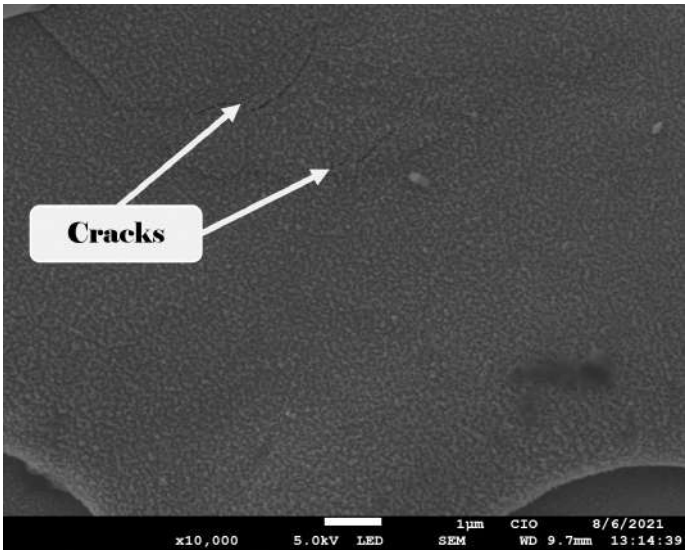

(b)

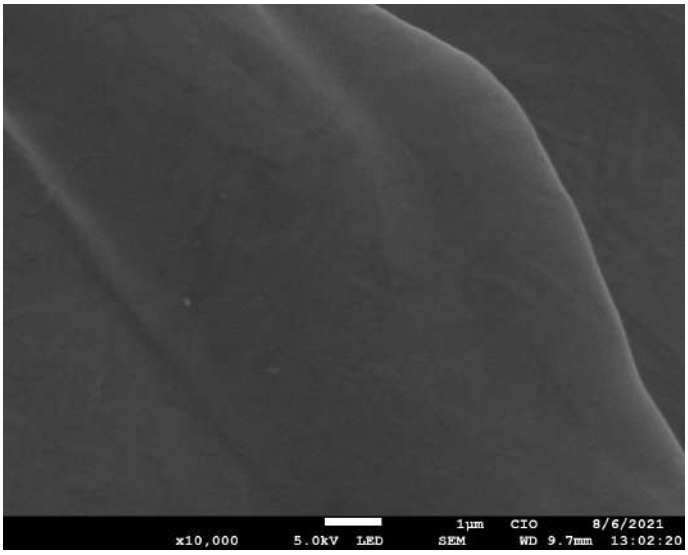

(c)

Figure 4.11: SEM micrographs of carbon steel samples with (a) for S_{f1}, (b)for S_{f2}, and (c) for S_{f3}.

The SEM images of both cleaned and uncleaned samples of grey cast iron are shown in **Figure 4.12**. We observed large crystal deposits on the surface of the uncleaned sample (**Figure 4.12a**) of up to 1.5 μm and cracks of up to 3 μm wide. Crystal deposits were however not observed on the cleaned samples. Nonetheless, some tiny cracks of about 200 nm were observed on the surface of the less cleaned sample (**Figure 4.12b**). The most cleaned sample as shown in **Figure 4.12c** had neither crystal deposits nor cracks. Further analysis of the sample's chemistry and surface roughness will be in this chapter's later sections.

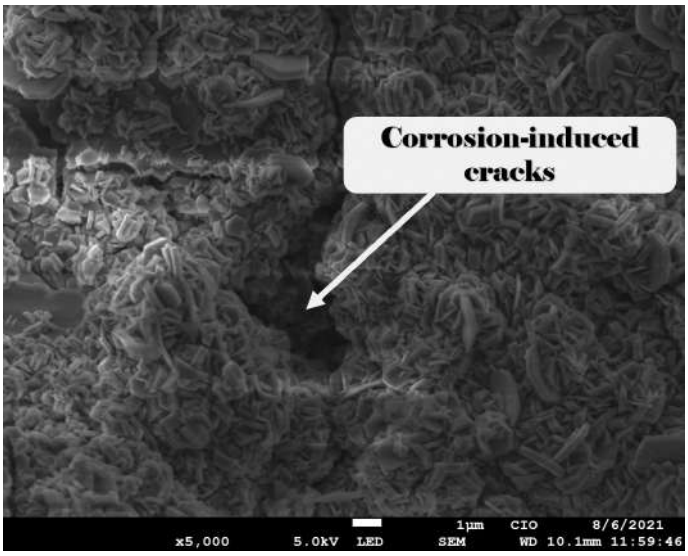

(a)

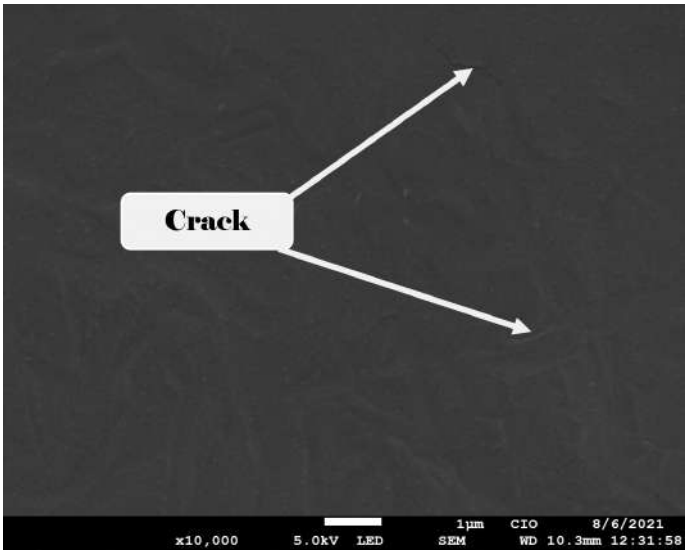

(b)

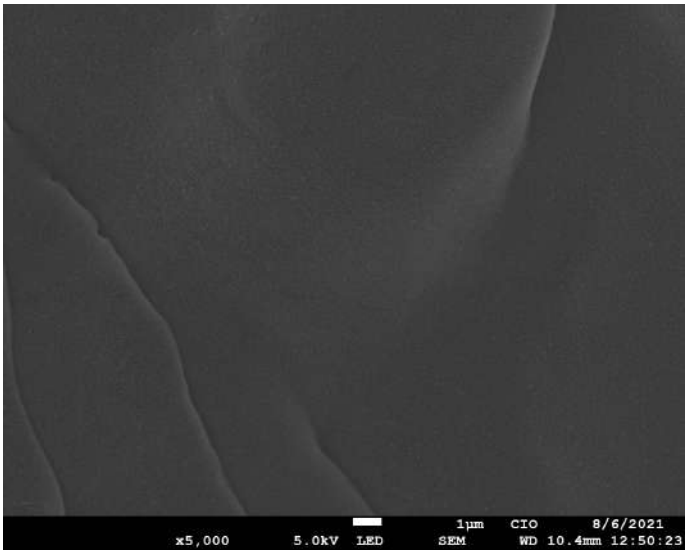

(c)

Figure 4.12: SEM micrographs of grey cast iron samples with (a) for R_{f1}, (b) for R_{f2}, and (c) for R_{f3}.

4.2.3.3 Raman Spectroscopy

Figure 4.13 shows the Raman spectrum of the uncleaned carbon steel sample S_{f1}. With reference from literature, the most profound oxides as revealed by the dominant peaks obtained for sample S_{f1} were a mixture of haematite ($\alpha - Fe_2O_3$), goethite ($\alpha - FeOOH$), siderite ($FeCO_3$), Wuestite (FeO), lepidocrocite ($\gamma - FeOOH$), and ferrihydrite ($(Fe^{3+})_2O_3 \cdot 0.5H_2O$). It should however be noted that the Raman characterization is only based upon a tiny surface area of the sample equivalent to the laser spot size in use. It is therefore not feasible to quantify the contribution of each phase. Rull *et al.*[133] established that naturally occurring haematite contains bands 224 and 410 which were also identified in our sample S_{f1}. These bands were however not spotted on samples S_{f2} and S_{f3} (**Figures 4.14** and **4.15**) respectively.

The Raman bands at 244 and 482 on sample S_{f1} are associated with goethite [133, 134]. However, these bands are hardly noticeable in samples S_{f2} and S_{f3}. This can be attributed to the low O/Fe ratios of the two samples as confirmed from the EDS analysis given in table **Table 4.5**. The band at 286 is an affirmation for the presence of siderite which is from the study conducted by Oh *et al.* [135] is a very stable mineral formed in carbon steel and easily detectable when moderated laser power is applied during spectroscopic analysis. The Raman bands associated with wuestite, lepidocrocite and ferrihydrite are 595, 650, and 711 respectively [135–138].

Lepidocrocite was also present on sample S_{f2} though with less intensity compared to the one spotted on sample S_{f1}. This can be attributed to the less percentage of oxide present on sample S_{f2} as confirmed from EDS results given in **Table 4.4** and the corresponding elemental ratios in **Table 4.5**. The presence of lepidocrocite in sample S_{f1} can also be evidenced by the results from Scanning Electron Microscope given in **Figure 4.11a**. Renato *et al.* [139] conducted a study to establish different forms of corrosion present on carbon steel and weathering steel exposed to three different environments for a given period of time, and results revealed that the carbon steel sample containing lepidocrocite had sandy-like crystals on the surface, which was also evident on our sample S_{f1}.

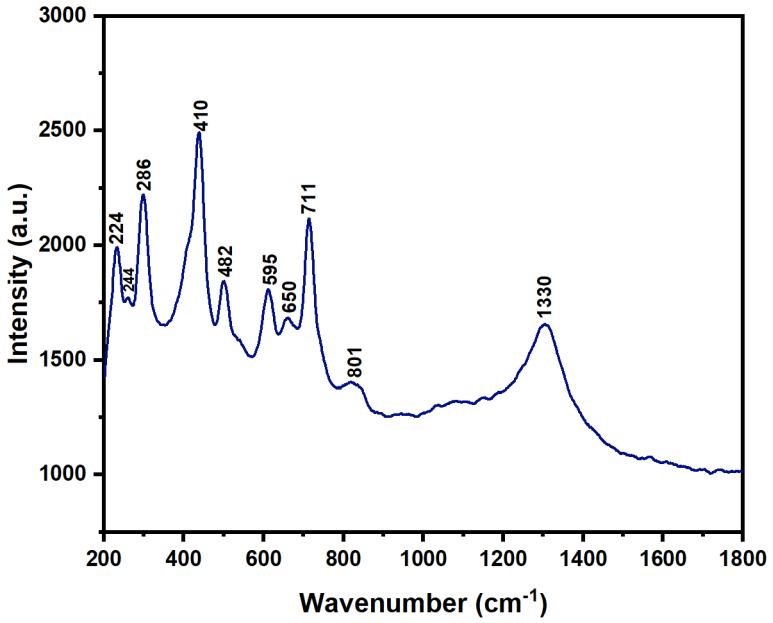

Figure 4.13: Raman spectrum of the uncleaned carbon steel sample S_{f1}.

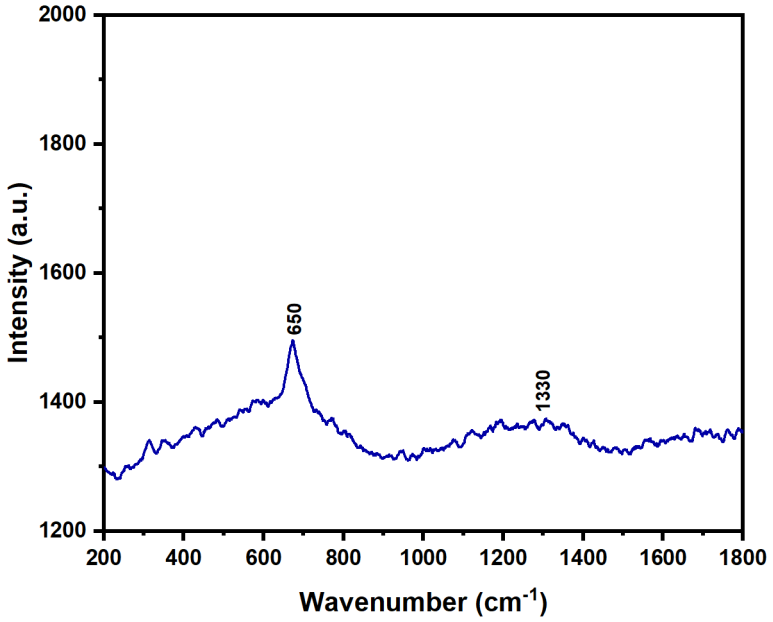

Figure 4.14: Raman spectrum of the less cleaned carbon steel sample S_{f2}.

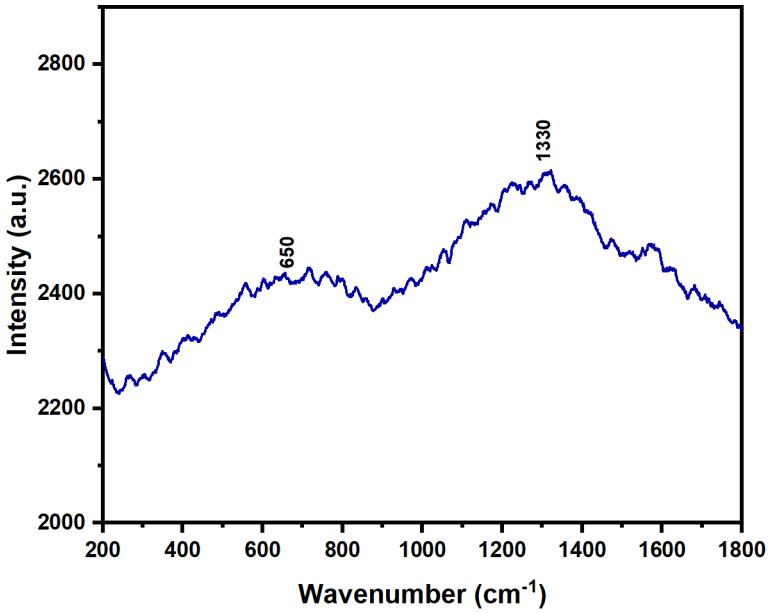

Figure 4.15: Raman spectrum of the most cleaned carbon steel sample S_{f3}.

Samples' normalized Raman spectra for S_{f1}, S_{f2} and S_{f3} given in **Figure 4.16** gives a clear understanding of how the oxide was eliminated from the surface of the most cleaned carbon steel (S_{f1}). We also noticed that a reduction in the intensity of the oxide led to a subsequent increase in the intensity of **C band**, **D band** and some **G band** also began to emerge. The **C band** is associated with carbon and our Raman spectra clearly indicate an amorphous carbon as evidenced by the wideband [140]. Muratahan *et al.* [141] established that amorphous surfaces have high ability to protect the material from further oxidation especially at ambient temperatures. This is due to the fact that amorphous films are excellent passivation layers because they "lack grain boundaries, dislocations, and other highly defective areas that would accelerate metal and/or oxygen ion transport kinetics" [142, 143]. This was also confirmed by our most cleaned sample that was able to withstand surface corrosion for a period as long as our research lasted.

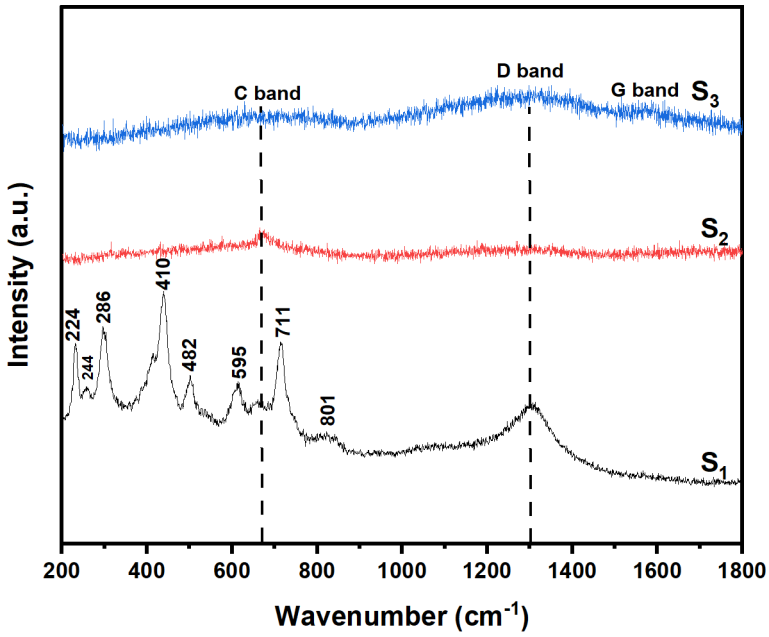

Figure 4.16: Normalized Raman spectra of the carbon steel samples S_{f1}, S_{f2} and S_{f3}.

Shown in **Figure 4.17** is the Raman spectrum of the uncleaned grey cast iron sample R_{f1}. The most dominant Raman bands were 223, 290, 410, 480, 650, and 680 which indicated a mixture of hematite, goethite, and lepidocrocite. These bands were also observed on the less cleaned sample (R_{f2}) as shown in **Figure 4.18**, though with lower intensity. This can be attributed to the lower percentage of oxide present on sample R_{f2} compared to that on R_{f1} as earlier confirmed from the EDS elemental analysis in **Table 4.6** and the subsequent O/Fe ratios in **Table 4.7**. No Raman bands containing hematite, goethite, and lepidocrocite were observed on sample R_{f3} as shown in **Figure 4.19**. We also observed the formation of the amorphous carbon which as mentioned earlier plays a pivotal role in buffering the cleaned surface against re-oxidation especially at ambient temperatures. This simply means sample R_{f3} is capable of withstanding corrosion for a significant amount of time, which was also confirmed during our experimental period.

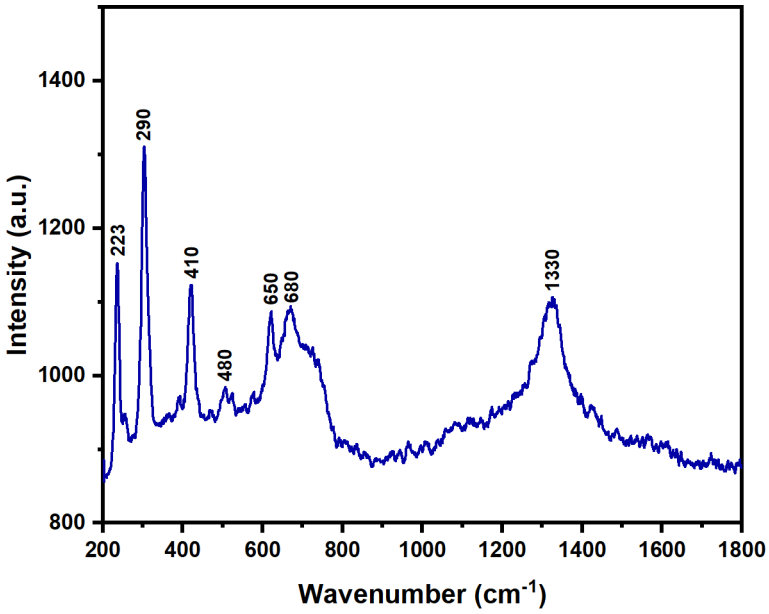

Figure 4.17: Raman spectrum of the uncleaned grey cast iron sample R_{f1}.

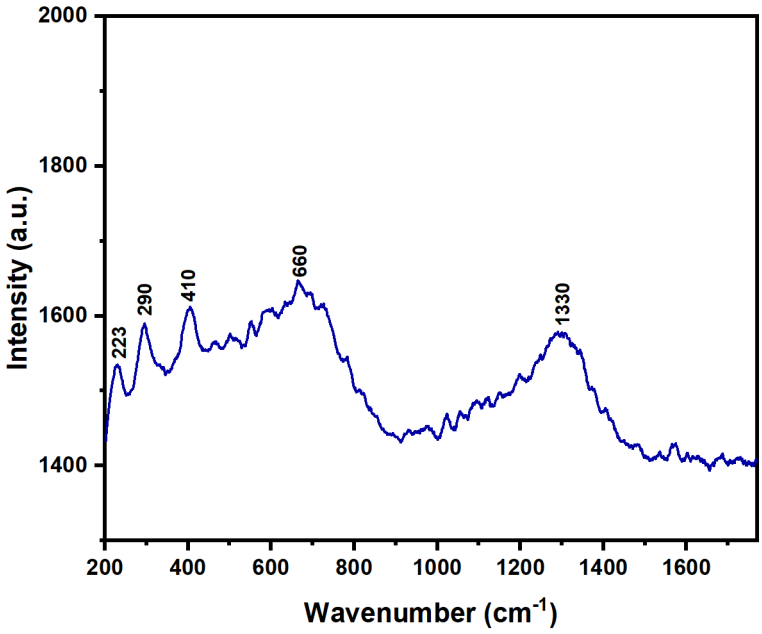

Figure 4.18: Raman spectrum of the less cleaned grey cast iron sample R_{f2}.

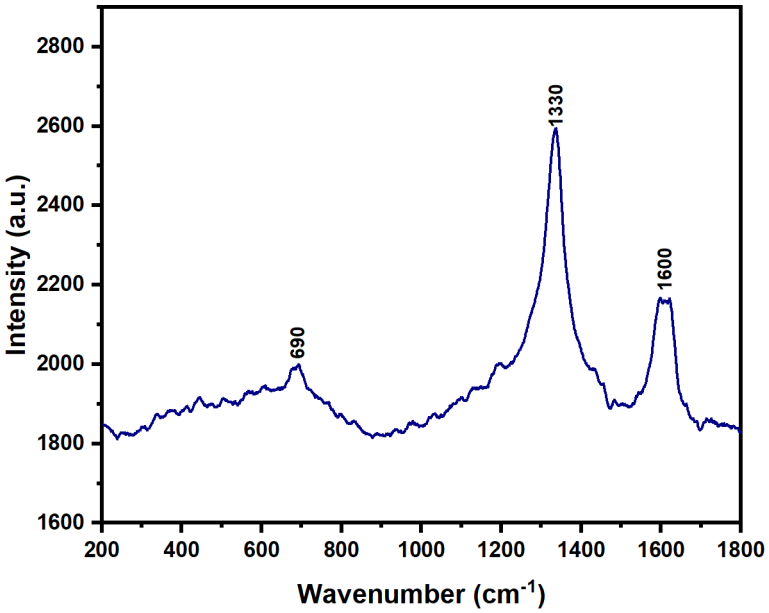

Figure 4.19: Raman spectrum of the most cleaned grey cast iron sample R_{f3}.

Graphene structure is measured by the intensity of the D/G bands. Because of the existence of structural flaws, the G band is produced by "in-plane vibrations of SP2-bonded carbon atoms", while the D band is produced by "out-of-plane vibrations" [144]. When comparing graphene and graphene oxide spectra, it will be noticed that the D band of graphene oxide is higher. As GO contains oxidative functional groups, this is caused by the breaking of SP2 bonds in the carbon atoms [145, 146]. In this regard, we analyzed the ratios of ID/IG for samples R_{f1}, R_{f2}, and R_{f3} to identify the magnitude of defects/cracks. The ratios of ID/IG were 1.507, 1.341, and 1.091 for the samples R_{f1}, R_{f2}, and R_{f3} respectively. This can also be justified based on the morphological SEM images for the three samples as shown in **Figure 4.12**. It was also evident that a decrease in the intensity of the oxide Raman bands led to a subsequent increase in the intensities of the **D band** and **G band** as shown in **Figure 4.20**.

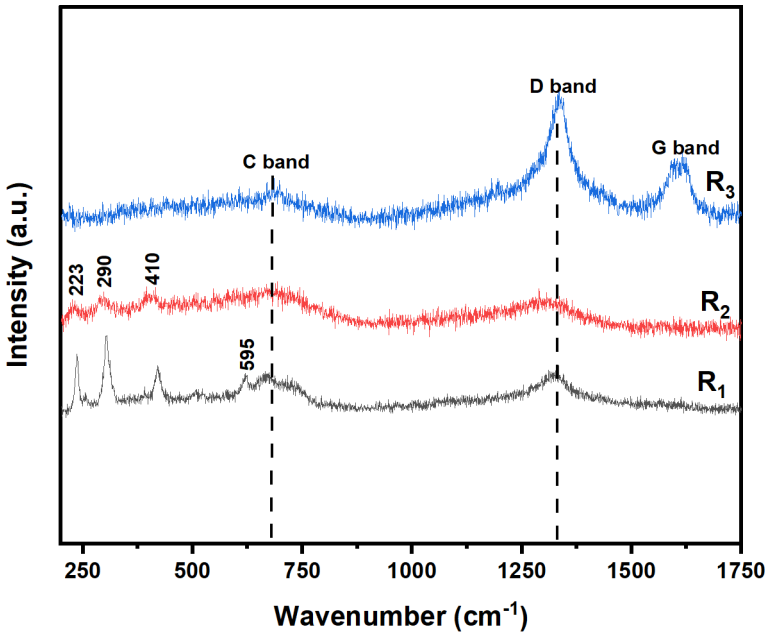

Figure 4.20: Normalized Raman spectra of the grey cast iron samples R_{f1}, R_{f2} and R_{f3}.

4.2.4 Chemical Composition

This section discusses the elements found in each sample. The analysis was performed using Energy Dispersive X-ray Spectrope found in SEM machine. In this case however, not all the elements found were analyzed. Our main focus was geared towards the composition of iron, carbon and oxygen and their relative abundance.

4.2.4.1 Energy Dispersive X-ray Spectroscopy (EDS)

The elemental composition of both cleaned and uncleaned samples was analyzed using EDS. It should however be noted that only elements bearing the highest percentage concentration will be discussed. **Table 4.4** Shows the concentration of Fe, C and O on samples S_{f1}, S_{f2}, and S_{f3}.

Table 4.4: X-ray diffraction spectroscopy (EDS) of carbon steel samples S_{f1}, S_{f2}, and S_{f3}.

Sample	Elemental Composition (wt%)		
	Fe	C	O
S_{f1}	52.7	23.4	19.0
S_{f2}	82.7	10.5	6.4
S_{f3}	89.6	7.7	2.3

From the results shown in **Table 4.4**, it was observed that the concentration of carbon and oxygen on all the samples (S_{f1}, S_{f2}, and S_{f3}) decreased while that of iron increased, soon after the cleaning process was carried out. For instance, the percentage of oxygen on sample S_{f1} was about 19%, that on S_{f2} was about 6%, while on S_{f3} was about 2%. The presence of a high percentage of oxygen on sample S_{f1} signifies corrosion resulting from an oxide of iron. A decrease in oxygen concentration means a decrease in the amount of oxide present in the sample. This makes sample S_{f2} the less cleaned, while S_{f3} the most cleaned.

It can also be noted that the less percentage of iron is due to high percentage of carbon and oxygen, and the converse is also true. The high percentage of oxide present on sample S_{f2} may be subject to the oxidation resulting from laser irradiation during the cleaning process since no rust was spotted on the sample's surface, depending on the optical microscope examination performed in the preceding section.

From **Table 4.5** the ratios of all the elemental composition of samples S_{f1}, S_{f2} and S_{f3} exhibit a decreasing trend. The ratio C/Fe decreases from 0.444 to 0.086 for the samples S_{f1} and S_{f3} respectively, signifying a subsequent decrease in the oxide during the cleaning process. We can also observe the high ratios of O/C for all the samples compared to the ratios of C/Fe and O/Fe. It is worth noting that the oxide of carbon does not pose any detriment as far as surface corrosion is concerned.

Table 4.5: Elemental ratios of the carbon steel samples S_{f1}, S_{f2}, and S_{f3}.

Sample	**Elemental Ratios**		
	C/Fe	O/C	O/Fe
S_{f1}	0.444	0.812	0.361
S_{f2}	0.127	0.610	0.077
S_{f3}	0.086	0.299	0.026

Shown in **Table 4.6** is the EDS analysis of the elemental composition of the grey cast iron samples R_{f1}, R_{f2} and R_{f3}. For the case of R_{f1}, no composition of carbon was spotted but rather, a small amount of silicon (not shown). We observed a decrease in carbon and oxygen composition and an increase in iron composition from samples R_{f1}, R_{f2} and R_{f3} respectively. This signified a decrease in the oxide of iron during the cleaning process. We should also recall that due to the graphitic microstructure of the gray cast iron, it wasn't possible for the laser beam to completely penetrate the surface pores and ablate all the corrosion for the case of the cleaned samples (R_{f2} and R_{f3}). This simply means that the percentage of oxide present on the surface of the two samples may be subject to the summation of corrosion and oxidation due to laser irradiation during the cleaning process. It should however be noted that

our most cleaned sample (R_{f3}) had less percentage of oxygen (about 3%) compared to the uncleaned (about 44%) and the less cleaned (about 6%) samples respectively (R_{f1} and R_{f2}).

Table 4.6: X-ray diffraction spectroscopy (EDS) of grey cast iron samples R_{f1}, R_{f2}, and R_{f3}.

Sample	Elemental Composition (wt%)		
	Fe	C	O
R_{f1}	50.4	–	44.7
R_{f2}	74.3	17.0	6.8
R_{f3}	84.0	11.2	3.2

From the analysis of the elemental ratios shown in **Table 4.6**, we observed a much similar trend as the one experienced for the case of carbon steel. The ratio O/Fe indicates a significant decrease from 0.887 to 0.038 for R_{f1} and R_{f3} respectively. This shows the high efficiency of the laser cleaning process. It should also be noted that oxide of carbon does not influence the corrosion of our cleaned samples as earlier mentioned.

Table 4.7: Elemental ratios of the cast iron samples R_{f1}, R_{f2}, and R_{f3}.

Sample	Elemental Ratios		
	C/Fe	O/C	O/Fe
R_{f1}	NaN	NaN	0.887
R_{f2}	0.229	0.400	0.092
R_{f3}	0.133	0.286	0.038

4.3 Simulation Results

Various simulation results obtained using our mathematical model are discussed here. A comparison between experimental and simulation results is also made so as to assess the effectiveness of the model used. The initial conditions for simulation was the ambient temperature (300 K).

4.3.1 Electron-Lattice Temperature Transition

The transformation of electron and lattice temperature was analyzed as given in **Figure 4.21**. As mentioned in chapter 3, the surface electrons interact with the

laser beam right upfront, after which the temperature is propagated to the bulk material (lattice).

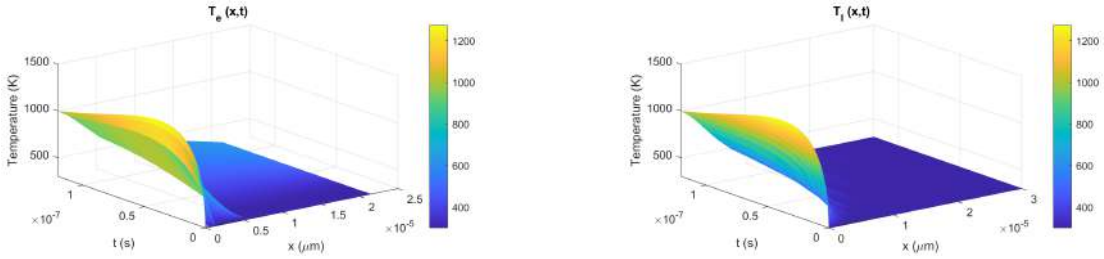

(a) **(b)**

Figure 4.21: Temperature transformation against time and ablation depth of the sample, (a) electron, and (b) lattice: numerical simulation of grey cast iron with laser wavelength of 1070 nm and fluence of 3.68 Jcm^{-2}

As observed in **Figures 4.21a** and **4.21b**, the electron and lattice temperatures are almost equal, with very slight difference ($T_e = 1274K$ and $T_l = 1262K$). This is due to the duration of the laser pulse's interaction with the sample (nanoseconds regime) [91]. This also indicates that a single temperature is enough to demonstrate the propagation of heat through the sample. Our model also indicates surface ablation at a temperature of 1274 K which is closer to the measured melting temperature of grey cast iron (1373 K) [147].

4.3.2 Phase Change Material (PCM)

When a material undergoes a process of phase transition, it releases enough energy to produce significant heating and cooling. A typical transition occurs between the first two states of matter, namely solid and liquid, with the third state of matter being in between. Phase transitions are characterized by a material's conformation to one crystalline structure, followed by conformation to another [148]. During laser interaction with the sample, the surface gets heated up faster than the bulk of the material. A significant increase in temperature causes melting. As the cooling of the surface takes place, the melted material is re-solidified.

Figures 4.22 and **4.23** shows a numerical simulation of the phase change for carbon steel and grey cast iron respectively. The maximum temperature is a result of the heat dissipation from the laser pulses during ablation process, some of which is absorbed by the sample. The average temperature, is the resultant amount of heat that will be gained by the sample once all other losses have been taken into account. We can observe a steady increase in temperature for the first 20 ns of the laser

interaction with the sample, after which the temperature decreases with time. The maximum temperature observed for the case of carbon steel was 1693 K while that of grey cast iron was 1434 K. These temperatures are both in conformity with the respective melting temperatures of each sample [147, 149]. During the cooling process, solidification of the sample takes place.

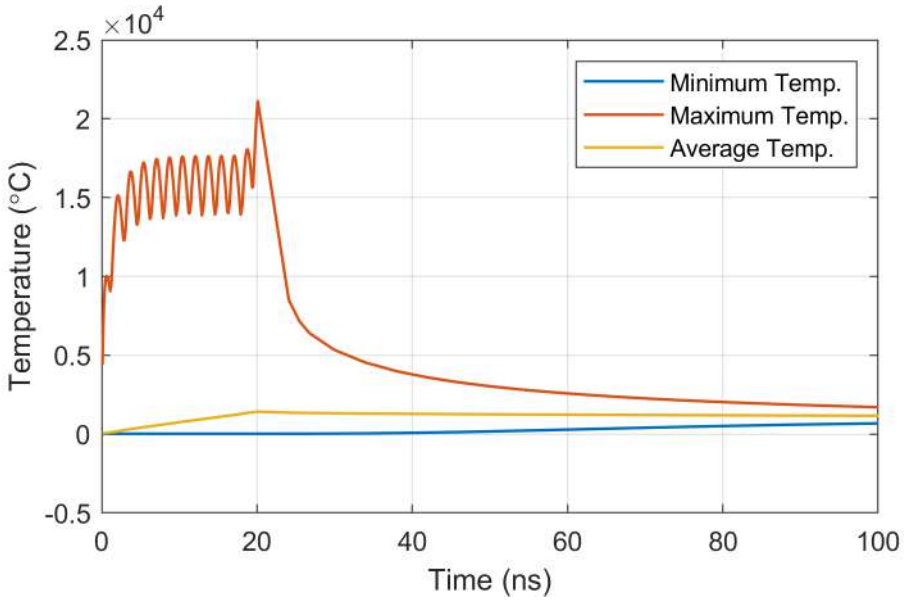

Figure 4.22: Phase transition of carbon steel during interaction with a laser pulse of wavelength 1070 nm and fluence of 6.44 Jcm^{-2}.

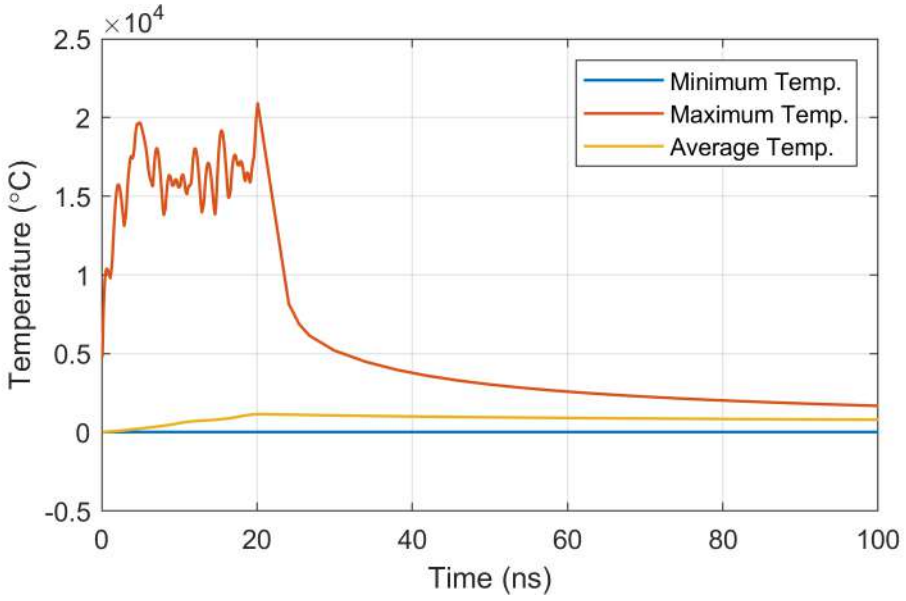

Figure 4.23: Phase transition of grey cast iron during interaction with a laser pulse of wavelength 1070 nm and fluence of 6.44 Jcm^{-2}.

4.3.3 Surface Microstructure

Using an optical microscope with a magnification greater than 25, the structure of a prepared material surface is exposed as microstructure [150]. If a material has a complex microstructure, it may have an impact on a wide range of physical characteristics, including toughness, ductility, and hardness. The microstructure can also have an impact on how well a material performs at extreme temperatures. These characteristics determines how materials are used for industrial purposes. As mentioned in chapter 3, our samples had varying microstructures. In this simulation therefore, we try to understand how heat is distributed on the surface of each sample. The surface of carbon steel was considered to be compact while that of grey cast iron had some micro-pittings.

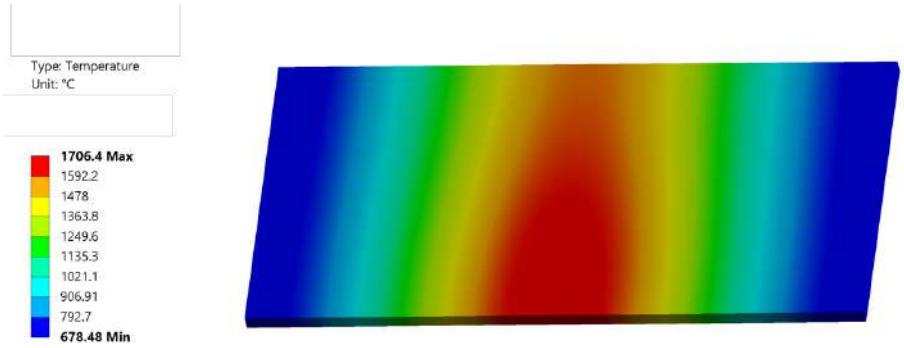

Figure 4.24: Heat distribution on the surface of carbon steel; numerical simulation with a laser pulse of wavelength 1070 nm and fluence of 6.44 Jcm^{-2}.

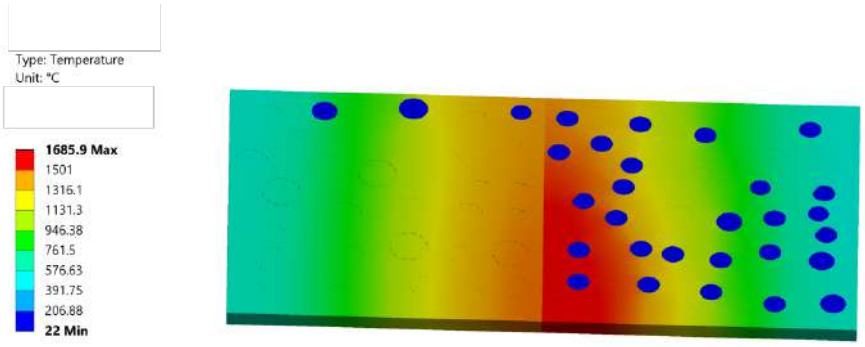

Figure 4.25: Heat distribution on the surface of grey cast iron; numerical simulation with a laser pulse of wavelength 1070 nm and fluence of 6.44 Jcm^{-2}.

We can observe a uniform heat distribution on the surface of carbon steel as shown in (**Figure 4.24**) and a heat distribution pattern that is non-homogeneous on the surface of grey cast iron (**Figure 4.25**). The sections on the surface of grey cast iron with micro-pittings (represented by blue circles) receive less heat from the laser

due to the increased distance from the beam focal point (which causes the beam to defocus). Less ablation takes place on the region where less heat is dissipated. This also implies that less or no rust removal will be observed. An experimental analysis of the cleaned samples as shown in **Figures 4.7** and **4.10** is in conformity with our simulation results.

4.3.4 Temperature and Depth of Penetration

Given in **Figure 4.26** is the variation of temperature and depth of penetration for a given laser pulse. At the time of the laser pulse's initiation on the surface of the sample, electrons gain heat energy. This energy penetrates to the lattice depending on several factors including reflectivity of the sample, roughness, fluence of the beam, pulse duration, wavelength among others [151].

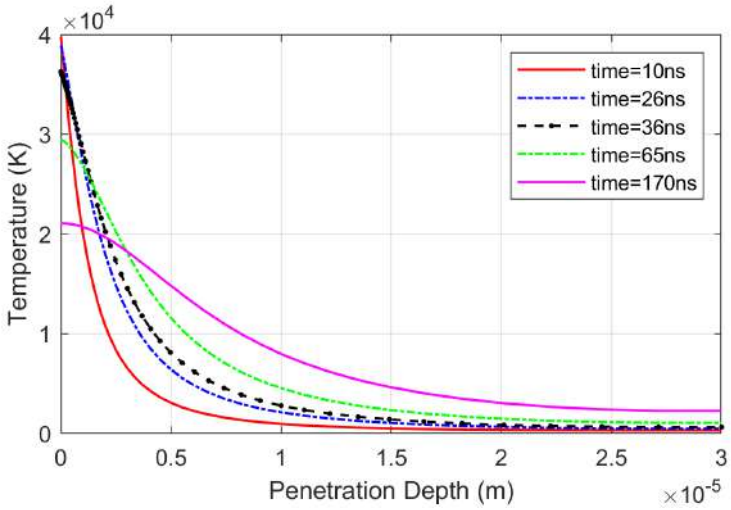

Figure 4.26: Variation of temperature and depth of penetration at different periods of the laser pulse; simulation of carbon steel with a laser of wavelength 1070 nm and fluence of 6.44 Jcm^{-2}.

Two trends can be noted in **Figure 4.26**. First, we can observe a decrease in temperature with an increase in depth of penetration for each period of time. This simply means that surface electrons lose a significant amount of heat to the interior electrons after the onset of the laser pulse. The second observation is about the period of the pulse. As time elapses, the electron temperature decreases [152]. The temperature rises rapidly when the laser pulse impacts the sample's surface. However, we can observe a significant decrease in temperature as time increases, which exemplifies a cooling process.

4.3.5 Temperature and Time

Figure 4.27 describes how the temperature of carbon steel varies with time at different depths. When the laser pulse first strikes the surface at a depth of 0 μm, there is an instantaneous increase in temperature to 8200 K before it starts decreasing with time. However, as the penetration depth increases from $0 - 5\mu m$, the temperature drops to a maximum of 4200 K.

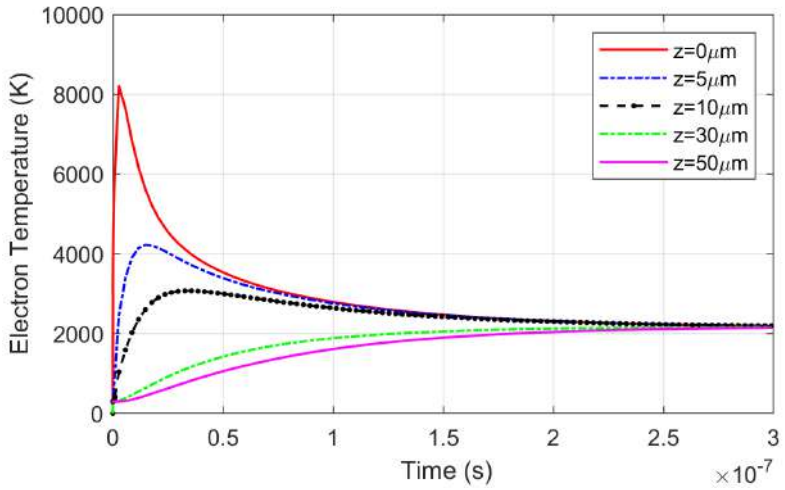

Figure 4.27: Variation of temperature and time at different depths of penetration; simulation of carbon steel with a laser of wavelength 1070 nm and fluence of 6.44 Jcm^{-2}.

4.3.6 Fluence and Depth of Penetration

Fluence of the incident laser beam determines the quantity of ablated material from the surface of the sample. **Figure 4.28** shows the variation of ablation depth with respect to fluence for the case of carbon steel.

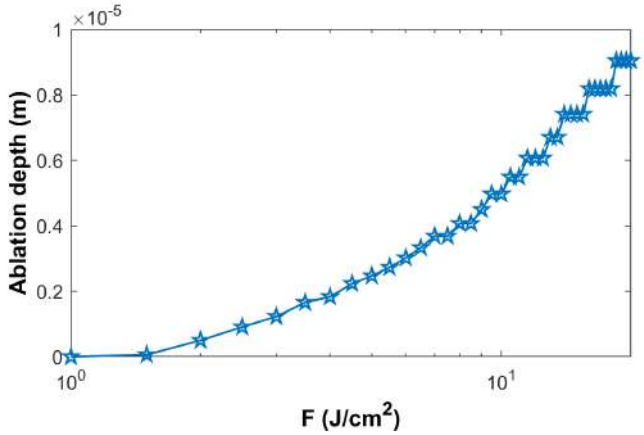

Figure 4.28: Variation of ablation depth versus fluence; numerical simulation of carbon steel with a laser of wavelength 1070 nm and maximum fluence of 15 Jcm^{-2}.

Table 4.8 shows a comparison between simulation and experimental values of the fluence with respective ablation depths. For instance, the fluence of 8.75 J/cm^2 resulted to ablation depth of 0.0502 and 0.04 mm for simulation and experimental respectively. This represents a difference of $\approx$ 10% which is much less compared to the literature where the values of 15% were found [153]. The experimental fluence was determined using Lidaris calculator.

Table 4.8: Comparison between simulation and experimental values of fluence and ablation depth of carbon steel samples.

Sample	**Fluence, F** (J/cm^2)	**Sim. Ablation,** X_{abl} **(mm)**	**Exp. Ablation,** X_{abl} **(mm)**
S_{f1}	–	–	–
S_{f2}	8.75	0.0502	0.04
S_{f3}	14.58	0.0815	0.07

Similarly, a comparison was also made to show the relationship between fluence and the depth of ablation for grey cast iron as shown in **Figure 4.29**.

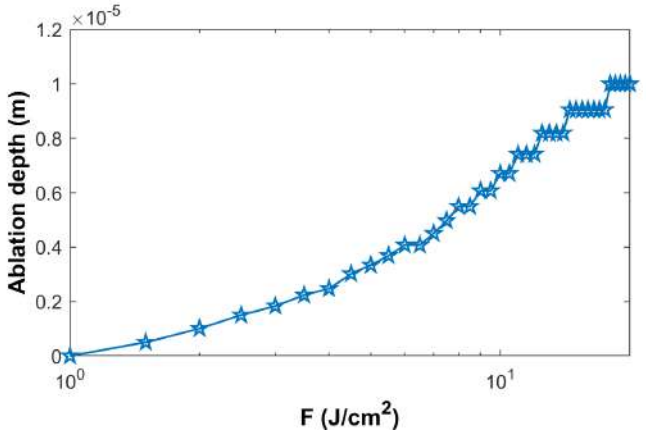

Figure 4.29: Variation of ablation depth versus fluence; numerical simulation of grey cast iron with a laser of wavelength 1070 nm and maximum fluence of 15 Jcm^{-2}.

As shown in **Table 4.9**, we can observe that sample R_2 which was cleaned with a fluence of 6.56 J/cm^2 had an ablation depth of 0.0726 and 0.06 mm for simulation and experimental values respectively. This represents a difference of $\approx$ 16% which less compared to 20% found in literature [154]. The values are also close, which further confirms the efficiency of our mathematical model.

Table 4.9: Comparison between simulation and experimental values of fluence and ablation depth of grey cast iron samples.

Sample	**Fluence, F** (J/cm^2)	**Sim. Ablation,** X_{abl} **(mm)**	**Exp. Ablation,** X_{abl} **(mm)**
R_{f1}	–	–	–
R_{f2}	6.56	0.0726	0.06
R_{f3}	14.58	0.103	0.09

Chapter 5

Conclusions and Recommendation

5.1 Conclusions

From the analysis of the results, it was possible to fulfill all the objectives stipulated in this research work. Low power nanosecond pulsed fiber laser was found to be the best for cleaning rust from metal surfaces compared to a low-power nanosecond pulsed carbon (IV) oxide laser. Rust removal requires high absorptivity since it forms part of the material's surface and must be melted for ablation to take place. In some studies, however, high power CO_2 laser has been utilized in de-rusting [132, 155]. This was not the case for our research since we sought to utilize low-power lasers that will not only provide the best cleaning parameters but also be economically viable. For this reason, all the samples analyzed in this research were cleaned using the fiber laser after the CO_2 laser failed to ablate the rust from the samples cleaned using it.

Using the mathematical simulation, it was possible to describe the mechanism of laser-material interaction that would otherwise be impossible to understand. This also enabled us to meticulously select the cleaning parameters that gave us the best results during the experimental process. It should however be understood that not all the thermodynamic processes taking place in the samples can be verified mathematically due to the complexity involved. We successfully described the phase change, variation of temperature with time as well as penetration depth, and justified the less ablation that took place inside the micro-pittings on the surface of grey cast iron during the cleaning process.

For carbon steel, the best cleaning parameters involved a pulse velocity of 1000 mm/s, line spacing of 30 μm, 15 scanning loops, an average power of 50 % ($\approx$ 11.5

W), and a pulse rate of 20 kHz. For the case of grey cast iron, the best parameters constituted pulse velocity of 750 mm/s, line spacing of 30 μm, 10 scan loops, 50 % of average power, and a pulse rate of 20 kHz. We noticed a high amount of surface oxidation on the less cleaned samples of both carbon steel and grey cast iron compared to the most cleaned samples resulting from laser irradiation. This was characterized by the presence of dark patches on the surface. The less cleaned samples also exhibited more surface roughness and less ability to withstand future re-oxidation when exposed to ambient environmental conditions. SEM micrographs also revealed the presence of micro-cracks and more surface defects on less cleaned samples as compared to the most cleaned samples. Finally, our most cleaned samples also exhibited less cleaning time compared to less cleaned ones, and this makes the entire choice of parameters economically suitable. Control of the laser parameters is therefore very critical in the cleaning process.

The type of oxides formed on both carbon steel and grey cast iron during the corrosion process were determined by Raman spectroscopy. For carbon steel, the main Raman bands were formed at 224, 286, 410, 482, 595, 650, and 711 which from literature comprised of a mixture of hematite, goethite, siderite, wuestite, lepidocrocite, and ferrihydrite. For grey cast iron, the main Raman bands were 223, 290, 410, 480, 650, and 680 which comprised of a mixture of hematite, goethite, and lepidocrocite. The results were also verified through SEM analysis. It is important to note that the type of oxide formed during the corrosion process has a significant effect on the choice of cleaning parameters.

The choice of material for laser cleaning is also critical. From the analysis of the results of carbon steel and grey cast iron samples, it was established that not all materials can be cleaned using laser irradiation. Although the physical appearance of the most cleaned sample of grey cast iron revealed fewer surface defects and no corrosion, further analysis using spectroscopic and microscopic techniques proved otherwise. A much defective surface of grey cast iron was discovered with some rust embedded inside the pores that could not be accessed by the laser beam during the cleaning process. Moreover, EDS analysis revealed a significantly high percentage of oxide on the surface of the most cleaned grey cast iron sample as opposed to the most cleaned carbon steel sample. The choice of material to be cleaned should therefore put into consideration a more compact microstructure that will enhance uniform distribution of the laser energy to guarantee the best results.

5.2 Recommendations for Future Work

Further research can be conducted to establish the surface characterization and surface analysis either through laser interaction or simulation by taking into account several laser parameters.

We also suggest an application of steam laser cleaning to materials possessing an irregular microstructure like grey cast iron as opposed to dry laser cleaning applied in this work. This will enhance cleaning efficiency. Additionally, low power CO_2 laser should also be experimented with the steam laser cleaning technique.

Bibliography

[1] M. Yamashita, H. Konishi, T. Kozakura, J. Mizuki, and H. Uchida, "In situ observation of initial rust formation process on carbon steel under na2so4 and nacl solution films with wet/dry cycles using synchrotron radiation x-rays," *Corrosion Science*, vol. 47, no. 10, pp. 2492–2498, 2005.

[2] X. H. Wang, "Study on a new formula for rust remover," in *Advanced Materials Research*, Trans Tech Publ, vol. 217, 2011, pp. 774–776.

[3] B. Hildebrant, A. I. Ndé-Tchoupé, M. Lufingo, T. Licha, and C. Noubactep, "Steel wool for water treatment: Intrinsic reactivity and defluoridation efficiency," *Processes*, vol. 8, no. 3, p. 265, 2020.

[4] C. Koehler and D. Torkelson, "Creative cleaning: Back to basics," 1993.

[5] S. H. Zaferani, M. Sharifi, D. Zaarei, and M. R. Shishesaz, "Application of eco-friendly products as corrosion inhibitors for metals in acid pickling processes–a review," *Journal of Environmental Chemical Engineering*, vol. 1, no. 4, pp. 652–657, 2013.

[6] V. Veiko, T. J. Mutin, V. Smirnov, E. Shakhno, and S. Batishche, "Laser cleaning of metal surfaces: Physical processes and applications," in *Fundamentals of laser assisted micro-and nanotechnologies*, International Society for Optics and Photonics, vol. 6985, 2008, p. 69850D.

[7] J. L. Bromberg, *The laser in America, 1950-1970*. MIT press, 1991.

[8] J.-P. Monchalin, "Progress towards the application of laser-ultrasonics in industry," in *Review of progress in quantitative nondestructive evaluation*, Springer, 1993, pp. 495–506.

[9] L. Sobotova and M. Badida, "Laser marking as environment technology," *Open Engineering*, vol. 7, no. 1, pp. 303–316, 2017.

[10] M. Ueda, Y. Saitoh, H. Hachisuka, H. Ishigaki, Y. Gokoh, and H. Mantani, "Studies on co2 laser marking," *Optics and Lasers in Engineering*, vol. 12, no. 4, pp. 245–249, 1990.

[11] H.-P. Berlien, *Applied laser medicine*. Springer Science & Business Media, 2003.

[12] J. Sofka, V. V. Nikulin, V. A. Skormin, D. H. Hughes, and D. J. Legare, "Laser communication between mobile platforms," *IEEE transactions on Aerospace and Electronic Systems*, vol. 45, no. 1, pp. 336–346, 2009.

[13] D. H. Titterton, *Military laser technology and systems*. Artech House, 2015.

[14] A. Fernandes and D. Kane, "An overview of experimental research into the laser cleaning of contaminants from surfaces," *Laser Cleaning II*, pp. 29–78, 2006.

[15] W. M. Steen and J. Mazumder, *Laser material processing*. springer science & business media, 2010.

[16] B. Lukyanchuk, *Laser cleaning: optical physics, applied physics and materials science*. World Scientific, 2002.

[17] P. Gargini, J. Glaze, and O. Williams, "The sia's 1997 national technology roadmap for semiconductors," *Solid state technology*, vol. 41, no. 1, pp. 73–76, 1998.

[18] W. Kern, "The evolution of silicon wafer cleaning technology," *Journal of the Electrochemical Society*, vol. 137, no. 6, p. 1887, 1990.

[19] B. Miller, C. W. Teutsch, and C. Fournier, "Detection and subsequent reduction of surface particle induced defects on silicon wafers," in *Particles on Surfaces 3*, Springer, 1991, pp. 153–171.

[20] W. Kern *et al.*, "Handbook of semiconductor wafer cleaning technology," *New Jersey: Noyes Publication*, pp. 111–196, 1993.

[21] K. Labuschagne and S. L. Pityana, "Laser induced damage threshold on metallic surfaces during laser cleaning," 2005.

[22] M. K. A. A. Razab, M. S. Jaafar, N. H. Abdullah, F. M. Suhaimi, M. Mohamed, N. Adam, N. A. A. N. Yusuf, *et al.*, "A review of incorporating nd: Yag laser cleaning principal in automotive industry," *Journal of radiation research and applied sciences*, vol. 11, no. 4, pp. 393–402, 2018.

[23] N. Antonopoulou-Athera, C. Kalathakis, E. Chatzitheodoridis, and A. Serafetinides, "Theoretical and experimental approach on laser cleaning of coins," *SN Applied Sciences*, vol. 1, no. 3, pp. 1–12, 2019.

[24] F. Brygo, C. Dutouquet, F. Le Guern, R. Oltra, A. Semerok, and J. Weulersse, "Laser fluence, repetition rate and pulse duration effects on paint ablation," *Applied surface science*, vol. 252, no. 6, pp. 2131–2138, 2006.

[25] V. Narayanan, R. K. Singh, and D. Marla, "Laser cleaning for rust removal on mild steel: An experimental study on surface characteristics," in *MATEC Web of Conferences*, EDP Sciences, vol. 221, 2018, p. 01 007.

[26] H. Yao, X. Zou, S. Zheng, Y. Hu, S. Zhang, C. Liang, H. Zhou, D. Wang, H. Wang, L. Yang, *et al.*, "Femtosecond laser-induced nanoporous layer for enhanced osteogenesis of titanium implants," *Materials Science and Engineering: C*, p. 112 247, 2021.

[27] A. C. Tam, W. P. Leung, W. Zapka, and W. Ziemlich, "Laser-cleaning techniques for removal of surface particulates," *Journal of Applied Physics*, vol. 71, no. 7, pp. 3515–3523, 1992.

[28] K. Imen, S. J. Lee, and S. D. Allen, "Laser-assisted micron scale particle removal," *Applied physics letters*, vol. 58, no. 2, pp. 203–205, 1991.

[29] W. Zapka, "The road to 'steam laser cleaning'," in *Laser Cleaning*, World Scientific, 2002, pp. 23–48.

[30] M. Mosbacher, N. Chaoui, J. Siegel, V. Dobler, J. Solis, J. Boneberg, C. N. Afonso, and P. Leiderer, "A comparison of ns and ps steam laser cleaning of si surfaces," *Applied Physics A*, vol. 69, no. 1, S331–S334, 1999.

[31] A. Kruusing, *Handbook of liquids-assisted laser processing*. Elsevier, 2010.

[32] P. Frank, F. Lang, M. Mosbacher, J. Boneberg, and P. Leiderer, "Infrared steam laser cleaning," *Applied Physics A*, vol. 93, no. 1, pp. 1–4, 2008.

[33] F. Lang, M. Mosbacher, and P. Leiderer, "Near field induced defects and influence of the liquid layer thickness in steam laser cleaning of silicon wafers," *Applied Physics A*, vol. 77, no. 1, pp. 117–123, 2003.

[34] A. J. Gross and T. R. Herrmann, "History of lasers," *World journal of urology*, vol. 25, no. 3, pp. 217–220, 2007.

[35] R. Ladenburg, B. Lewis, R. Pease, and H. Taylor, "High speed aerodynamics and jet propulsion. volume ix. physical measurements in gas dynamics and combustion.," PRINCETON UNIV NJ, Tech. Rep., 1954.

[36] S. Clark, J. Donaldson, and S. Grimes, "Mössbauer spectroscopy," *Annual Reports Section" C"(Physical Chemistry)*, vol. 78, pp. 93–136, 1981.

[37] H. Theissing, P. Caplan, F. Dieter, and N. Rabbiner, "Optical pumping in crystals," *Physical Review Letters*, vol. 3, no. 10, p. 460, 1959.

[38] A. H. Rawicz, "Theodore harold maiman and the invention of laser," in *Photonics, Devices, and Systems IV*, International Society for Optics and Photonics, vol. 7138, 2008, p. 713 802.

[39] T. H. Maiman, T. H. Maiman, and Holland, *Laser Inventor*. Springer, 2018.

[40] K. Shimoda, *Introduction to laser physics*. Springer, 2013, vol. 44.

[41] S. John and G. Pang, "Theory of lasing in a multiple-scattering medium," *Physical Review A*, vol. 54, no. 4, p. 3642, 1996.

[42] G. S. He, Y. Cui, M. Yoshida, and P. N. Prasad, "Phase-conjugate backward stimulated emission from a two-photon-pumped lasing medium," *Optics letters*, vol. 22, no. 1, pp. 10–12, 1997.

[43] A. Saini, *Laser*, `https://www.slideshare.net/ankushsaini123/6933laser-p-pts`, Dec. 2011.

[44] R. Powell, "Types of lasers," *Springer Handbook of Atomic*, p. 1035, 2006.

[45] K. F. Renk, *Basics of laser physics*. Springer, 2012.

[46] A. Mirhashemi, N. Sharifi, M. Moharrami, and N. Chiniforush, "Evaluation of different types of lasers in surface conditioning of porcelains: A review article," *Journal of lasers in medical sciences*, vol. 8, no. 3, p. 101, 2017.

[47] S. Takac, S. Stojanović, and B. Muhi, "Types of medical lasers," *Medicinski pregled*, vol. 51, no. 3-4, pp. 146–150, 1998.

[48] A. Yariv *et al.*, *Optical electronics in modern communications*. Oxford University Press, USA, 1997, vol. 1.

[49] M. Normand, *Lc laser droplets and flexible nanocomposite materials.* `https://www.eng.ed.ac.uk/about/events/20171004-1230/imns-seminar-lc-laser-droplets-and-flexible-nanocomposite-materials`, Oct. 2017.

[50] F. J. Duarte, *High power dye laser*, `www.tunablelasers.com.Retrieved19April2018.`, Nov. 2021.

[51] F. J. Duarte and L. W. Hillman, "Dye laser principles, with applications," 1990.

[52] W. Demtröder, "Spectroscopic instrumentation," in *Laser Spectroscopy*, Springer, 2003, pp. 97–219.

[53] O. Svelto and D. C. Hanna, *Principles of lasers*. Springer, 2010, vol. 1.

[54] D. Piccolo, D. Kostaki, and G. Crisman, *Quick Guide to Dermoscopy in Laser and IPL Treatments*. Springer, 2020.

[55] W. J. Witteman, *The CO2 laser*. Springer, 2013, vol. 53.

[56] E. 360, *Carbon dioxide lasers information*, `https://www.globalspec.com/learnmore/optical_components_optics/lasers/carbon_dioxide_lasers`, Nov. 2021.

[57] DAEnotes, *The molecular gas laser*, https://www.daenotes.com/electronics/microwave-radar/co2-gas-laser, Nov. 2021.

[58] D. Basting, F. Schäfer, and B. Steyer, "A simple, high power nitrogen laser," *Opto-electronics*, vol. 4, no. 1, pp. 43–49, 1972.

[59] F. R. Karl, *Basics of Laser Physics For Students of Science and Engineering*. Spinger, 2017.

[60] S. Saikan, "Nitrogen-laser-pumped single-mode dye laser," *Applied physics*, vol. 17, no. 1, pp. 41–44, 1978.

[61] Shabbusharma, *Nd yag laser working*, https://physicswave.com/nd-yag-laser-working/, May 2020.

[62] C. G. Technologies., *Nitrogen generators for laser cutting*. https://nitrogen-generators.com/nitrogen-generators-laser-cutting-applications/, Oct. 2021.

[63] K. Murray, *Nitrogen laser*, https://commons.wikimedia.org/w/index.php?curid=1932238, Jun. 2008.

[64] N. G. Basov, V. Danilychev, and Y. M. Popov, "Stimulated emission in the vacuum ultraviolet region," *Soviet Journal of quantum electronics*, vol. 1, no. 1, p. 18, 1971.

[65] H. Koehler, L. Ferderber, D. Redhead, and P. Ebert, "Stimulated vuv emission in high-pressure xenon excited by high-current relativistic electron beams," *Applied Physics Letters*, vol. 21, no. 5, pp. 198–200, 1972.

[66] V. Srinivasan, M. A. Smrtic, and S. Babu, "Excimer laser etching of polymers," *Journal of applied physics*, vol. 59, no. 11, pp. 3861–3867, 1986.

[67] H. Abramczyk, *Introduction to laser spectroscopy*. Elsevier, 2005.

[68] P. Kanerva, *Sparse distributed memory*. MIT press, 1988.

[69] GamLaser, *Krf excimer laser*, http://www.gamlaser.com/EX100.htm, Jun. 2021.

[70] B. J. Orr, "Infrared lidar applications in atmospheric monitoring," *Encyclopedia of Analytical Chemistry: Applications, Theory and Instrumentation*, pp. 1–49, 2006.

[71] R. G. Knollenberg, "Prospects for the helium-neon laser through the end of the century," in *Design of Optical Systems Incorporating Low Power Lasers*, International Society for Optics and Photonics, vol. 741, 1987, pp. 2–30.

[72] A. Javan, W. R. Bennett Jr, and D. R. Herriott, "Population inversion and continuous optical maser oscillation in a gas discharge containing a he-ne mixture," *Physical Review Letters*, vol. 6, no. 3, p. 106, 1961.

[73] J. Haus and R. Schaefer, "Sensors, optical," *The Optics Encyclopedia: Basic Foundations and Practical Applications*, 2007.

[74] F. X. Kaertner, L. R. Brovelli, D. Kopf, M. Kamp, I. G. Calasso, and U. Keller, "Control of solid state laser dynamics by semiconductor devices," *Optical Engineering*, vol. 34, no. 7, pp. 2024–2036, 1995.

[75] T. H. Maiman *et al.*, "Stimulated optical radiation in ruby," 1960.

[76] T. George, L. Slama, M. Yokoyama, and L. Goldstein, "Scattering of ruby-laser beam by gases.," *Physical Review Letters*, vol. 14, no. 2, p. 54, 1965.

[77] R. V. Pole and H. Wieder, "Continuous operation of a ruby laser during pumping pulse," *Applied Optics*, vol. 3, no. 9, pp. 1086–1087, 1964.

[78] Britannica, *Ruby laser*, `https://www.britannica.com/technology/ruby-laser`, Jun. 1996.

[79] W. Koechner, *Solid-state laser engineering*. Springer, 2013, vol. 1.

[80] J. Geusic, H. Marcos, and L. Van Uitert, "Laser oscillations in nd-doped yttrium aluminum, yttrium gallium and gadolinium garnets," *Applied Physics Letters*, vol. 4, no. 10, pp. 182–184, 1964.

[81] A. Penzkofer, "Solid state lasers," *Progress in Quantum Electronics*, vol. 12, no. 4, pp. 291–427, 1988.

[82] A. Ikesue, K. Kamata, and K. Yoshida, "Effects of neodymium concentration on optical characteristics of polycrystalline nd: Yag laser materials," *Journal of the American Ceramic Society*, vol. 79, no. 7, pp. 1921–1926, 1996.

[83] M. Schellhorn, "High-power diode-pumped tm: Ylf laser," *Applied Physics B*, vol. 91, no. 1, pp. 71–74, 2008.

[84] R. Fields, M. Birnbaum, and C. Fincher, "Highly efficient nd: Yvo4 diode-laser end-pumped laser," *Applied physics letters*, vol. 51, no. 23, pp. 1885–1886, 1987.

[85] E. Snitzer and R. Woodcock, "Yb3+–er3+ glass laser," *Applied Physics Letters*, vol. 6, no. 3, pp. 45–46, 1965.

[86] E. Mind, *Construction of neodymium-yttrium-aluminium-garnet laser, physics*, `http://www.expertsmind.com/questions/construction-of-neodymium-yttrium-aluminium-garnet-laser-301103262.aspx`, Jun. 2005.

[87] B. Abaie, E. Mobini, S. Karbasi, T. Hawkins, J. Ballato, and A. Mafi, "Random lasing in an anderson localizing optical fiber," *Light: Science & Applications*, vol. 6, no. 8, e17041–e17041, 2017.

[88] C. J. Koester and E. Snitzer, "Amplification in a fiber laser," *Applied optics*, vol. 3, no. 10, pp. 1182–1186, 1964.

[89] J. Yang, Y. Tang, and J. Xu, "Development and applications of gain-switched fiber lasers," *Photonics Research*, vol. 1, no. 1, pp. 52–57, 2013.

[90] V. Gapontsev and L. Samartsev, "High-power fiber laser," in *Advanced Solid State Lasers*, Optical Society of America, 1990, LSR1.

[91] J. P. Davim, *Laser in manufacturing*. John Wiley & Sons, 2013.

[92] T. m. Pollak, W. Wing, R. Grasso, E. Chicklis, and H. Jenssen, "Cw laser operation of nd: Ylf," *IEEE Journal of Quantum Electronics*, vol. 18, no. 2, pp. 159–163, 1982.

[93] W. T. Silfvast, *Laser fundamentals*. Cambridge university press, 2004.

[94] S. Martellucci, A. N. Chester, and A. V. Scheggi, *Laser applications for mechanical industry*. Springer Science & Business Media, 2012, vol. 238.

[95] M. v. Allemen and A. Bllatter, *Laser-beam interaction with materials*, 1995.

[96] R. M. Wood, *Laser-induced damage of optical materials*. CRC Press, 2003.

[97] N. Bloembergen, "Laser-induced electric breakdown in solids," *IEEE Journal of Quantum Electronics*, vol. 10, no. 3, pp. 375–386, 1974.

[98] J. Han, Y. Li, Q. Zhang, Y. Fu, W. Fan, G. Feng, L. Yang, X. Xie, Q. Zhu, and S. Zhou, "Phase explosion induced by high-repetition rate pulsed laser," *Applied surface science*, vol. 256, no. 22, pp. 6649–6654, 2010.

[99] B. Stuart, M. Feit, S. Herman, A. Rubenchik, B. Shore, and M. Perry, "Nanosecond-to-femtosecond laser-induced breakdown in dielectrics," *Physical review B*, vol. 53, no. 4, p. 1749, 1996.

[100] X. Wang, X. Ye, H. Yao, P. Wei, F. Yin, J. Cong, Y. Tong, L. Zhang, and W. Zhu, "Simulation of femtosecond laser ablation and spallation of titanium film based on two-temperature model and molecular dynamics," *Journal of Laser Applications*, vol. 33, no. 1, p. 012 047, 2021.

[101] N. Firouzi Farrashbandi and M. Eslami-Kalantari, "Inverse bremsstrahlung absorption in laser-fusion plasma," *Journal of Theoretical and Applied Physics*, vol. 14, no. 3, pp. 261–264, 2020.

[102] D. Bleiner and A. Bogaerts, "Multiplicity and contiguity of ablation mechanisms in laser-assisted analytical micro-sampling," *Spectrochimica Acta Part B: Atomic Spectroscopy*, vol. 61, no. 4, pp. 421–432, 2006.

[103] J. H. Yoo, S. Jeong, R. Greif, and R. Russo, "Explosive change in crater properties during high power nanosecond laser ablation of silicon," *Journal of Applied physics*, vol. 88, no. 3, pp. 1638–1649, 2000.

[104] P. Mulser and D. Bauer, *High power laser-matter interaction*. Springer, 2010, vol. 238.

[105] V. Mosorov, "The lambert-beer law in time domain form and its application," *Applied Radiation and Isotopes*, vol. 128, pp. 1–5, 2017.

[106] H. J. Geijselaers and H. Huetink, "Finite element analysis of transformation hardening," in *Proceedings of the fifth International conference on Numerical Methods in Industrial Forming Processes*, 1995, pp. 681–685.

[107] P. Sidles and G. Danielson, "Thermal diffusivity of metals at high temperatures," *Journal of Applied Physics*, vol. 25, no. 1, pp. 58–66, 1954.

[108] R. Wilson, B. A. Apgar, L. W. Martin, and D. G. Cahill, "Thermoreflectance of metal transducers for optical pump-probe studies of thermal properties," *Optics express*, vol. 20, no. 27, pp. 28 829–28 838, 2012.

[109] D. Larcombe, "Fiber versus co2 laser cutting," *Industrial Laser Solutions*, vol. 13, no. 11, 2013.

[110] J. F. Shackelford, Y.-H. Han, S. Kim, and S.-H. Kwon, *CRC materials science and engineering handbook*. CRC press, 2016.

[111] M. F. Ashby, H. Shercliff, and D. Cebon, *Materials: engineering, science, processing and design*. Butterworth-Heinemann, 2018.

[112] M. Eberhart, *Why things break: understanding the world by the way it comes apart*. Crown, 2007.

[113] D. R. Gaskell and D. E. Laughlin, *Introduction to the Thermodynamics of Materials*. CRC press, 2017.

[114] A. Barchanski, *Laser-Generated Functional Nanoparticle Bioconjugates*. Springer, 2016.

[115] Thorlabs, *F-theta scan lenses*, `https://www.thorlabs.com/newgrouppage9.cfm?objectgroup_id=6430`, Mar. 2021.

[116] M.-M. Fu, P.-F. Chen, Y. Wang, and H.-Y. Jiang, "Optical design of super wide angle f-theta lens with large operation area," *Yingyong Guangxue(Journal of Applied Optics)*, vol. 32, no. 6, pp. 1083–1087, 2011.

[117] M. Colina, C. Molpeceres, M. Morales, F. Allens-Perkins, G. Guadaño, and J. Ocana, "Laser ablation modelling of aluminium, silver and crystalline silicon for applications in photovoltaic technologies," *Surface Engineering*, vol. 27, no. 6, pp. 414–423, 2011.

[118] W. Napadłek, A. Woźniak, and C. Pakowski, "The properties of cast iron surface layers modified by laser ablation micromachining," *Tribologia*, 2017.

[119] C. E. Webb and J. D. Jones, *Handbook of Laser Technology and Applications: Laser design and laser systems*. CRC Press, 2004, vol. 2.

[120] S. Anisimov, B. Kapeliovich, T. Perelman, *et al.*, "Electron emission from metal surfaces exposed to ultrashort laser pulses," *Zh. Eksp. Teor. Fiz*, vol. 66, no. 2, pp. 375–377, 1974.

[121] D. Liu, C. Chen, B. Man, X. Meng, Y. Sun, and F. Li, "Experimental investigation and 3d-simulation of the ablated morphology of titanium surface using femtosecond laser pulses," *The European Physical Journal Applied Physics*, vol. 72, no. 3, p. 31 301, 2015.

[122] D. Lopez, W. d. Schreiner, S. De Sánchez, and S. Simison, "The influence of carbon steel microstructure on corrosion layers: An xps and sem characterization," *Applied Surface Science*, vol. 207, no. 1-4, pp. 69–85, 2003.

[123] L. Collini, G. Nicoletto, and R. Konečná, "Microstructure and mechanical properties of pearlitic gray cast iron," *Materials Science and Engineering: A*, vol. 488, no. 1-2, pp. 529–539, 2008.

[124] A. Tofini, L. Levesque, O. Lebel, and R. G. Sabat, "Erasure of surface relief gratings in azobenzene molecular glasses by localized heating using a co 2 laser," *Journal of Materials Chemistry C*, vol. 6, no. 5, pp. 1083–1091, 2018.

[125] S. Janasekaran, M. Jamaludin, M. Muhamad, F. Yusof, and M. Abdul Shukor, "Autogenous double-sided t-joint welding on aluminum alloys using low power fiber laser.," *International Journal of Advanced Manufacturing Technology*, vol. 90, 2017.

[126] A. Kermanpur, S. Mahmoudi, and A. Hajipour, "Numerical simulation of metal flow and solidification in the multi-cavity casting moulds of automotive components," *Journal of Materials Processing Technology*, vol. 206, no. 1-3, pp. 62–68, 2008.

[127] T. R. Vijayaram, S. Sulaiman, A. Hamouda, and M. Ahmad, "Numerical simulation of casting solidification in permanent metallic molds," *Journal of materials processing technology*, vol. 178, no. 1-3, pp. 29–33, 2006.

[128] S. Luo, M. Zhu, and S. Louhenkilpi, "Numerical simulation of solidification structure of high carbon steel in continuous casting using cellular automaton method," *ISIJ international*, vol. 52, no. 5, pp. 823–830, 2012.

[129] C. Zheng, N. Xiao, L. Hao, D. Li, and Y. Li, "Numerical simulation of dynamic strain-induced austenite–ferrite transformation in a low carbon steel," *Acta Materialia*, vol. 57, no. 10, pp. 2956–2968, 2009.

[130] *Surface morphology*, en, https://www.nanolabtechnologies.com/Surface-Morphology/, Accessed: 2022-3-15, Apr. 2018.

[131] L. Alvarenga, "Super-resolution microscopy comes into focus: Sharper images, says olympus, are obtained if filtering algorithms are improved," *Genetic Engineering & Biotechnology News*, vol. 40, no. 1, pp. 60–62, 2020.

[132] Y. Ogbekene, P. Shukla, Y. Zhang, X. Shen, S. Prabhakaran, S. Kalainathan, K. Gulia, and J. Lawrence, "Laser cleaning of grey cast iron automotive brake disc: Rust removal and improvement in surface integrity," 2018.

[133] F. Rull, J. Martinez-Frias, A. Sansano, J. Medina, and H. Edwards, "Comparative micro-raman study of the nakhla and vaca muerta meteorites," *Journal of Raman Spectroscopy*, vol. 35, no. 6, pp. 497–503, 2004.

[134] M. Hanesch, H. Stanjek, and N. Petersen, "Thermomagnetic measurements of soil iron minerals: The role of organic carbon," *Geophysical Journal International*, vol. 165, no. 1, pp. 53–61, 2006.

[135] S. J. Oh, D. Cook, and H. Townsend, "Characterization of iron oxides commonly formed as corrosion products on steel," *Hyperfine interactions*, vol. 112, no. 1, pp. 59–66, 1998.

[136] P. Tan, J. Zhang, X. Wang, G. Zhang, and E. Wang, "Raman scattering from an individual tubular graphite cone," *Carbon*, vol. 5, no. 45, pp. 1116–1119, 2007.

[137] R. J. Thibeau, C. W. Brown, and R. H. Heidersbach, "Raman spectra of possible corrosion products of iron," *Applied Spectroscopy*, vol. 32, no. 6, pp. 532–535, 1978.

[138] G. Goya, T. Berquo, F. Fonseca, and M. Morales, "Static and dynamic magnetic properties of spherical magnetite nanoparticles," *Journal of applied physics*, vol. 94, no. 5, pp. 3520–3528, 2003.

[139] R. A. Antunes, I. Costa, and D. L. A. d. Faria, "Characterization of corrosion products formed on steels in the first months of atmospheric exposure," *Materials research*, vol. 6, no. 3, pp. 403–408, 2003.

[140] M. A. Tamor and W. Vassell, "Raman "fingerprinting"of amorphous carbon films," *Journal of Applied Physics*, vol. 76, no. 6, pp. 3823–3830, 1994.

[141] M. Aykol and K. A. Persson, "Oxidation protection with amorphous surface oxides: Thermodynamic insights from ab initio simulations on aluminum," *ACS applied materials & interfaces*, vol. 10, no. 3, pp. 3039–3045, 2018.

[142] A. Revesz and F. Fehlner, "The role of noncrystalline films in the oxidation and corrosion of metals," *Oxidation of metals*, vol. 15, no. 3, pp. 297–321, 1981.

[143] F. P. Fehlner and N. F. Mott, "Low-temperature oxidation," *Oxidation of metals*, vol. 2, no. 1, pp. 59–99, 1970.

[144] I. Childres, L. A. Jauregui, W. Park, H. Cao, Y. P. Chen, *et al.*, "Raman spectroscopy of graphene and related materials," *New developments in photon and materials research*, vol. 1, pp. 1–20, 2013.

[145] A. K. Gupta, Y. Tang, V. H. Crespi, and P. C. Eklund, "Nondispersive raman d band activated by well-ordered interlayer interactions in rotationally stacked bilayer graphene," *Physical Review B*, vol. 82, no. 24, p. 241 406, 2010.

[146] K.-i. Sasaki, Y. Tokura, and T. Sogawa, "The origin of raman d band: Bonding and antibonding orbitals in graphene," *Crystals*, vol. 3, no. 1, pp. 120–140, 2013.

[147] C. Cui, Z. Guo, H. Wang, and J. Hu, "In situ tic particles reinforced grey cast iron composite fabricated by laser cladding of ni–ti–c system," *Journal of Materials Processing Technology*, vol. 183, no. 2-3, pp. 380–385, 2007.

[148] C. Gau and R. Viskanta, "Melting and solidification of a pure metal on a vertical wall," 1986.

[149] J. Sinczak, W. Lapkowski, and S. Rusz, "Isothermal plastic forming of high melting temperature alloys," *Journal of materials processing technology*, vol. 72, no. 3, pp. 429–433, 1997.

[150] G. F. Vander Voort, S. R. Lampman, B. R. Sanders, G. J. Anton, C. Polakowski, J. Kinson, K. Muldoon, S. D. Henry, and W. W. Scott Jr, "Asm handbook," *Metallography and microstructures*, vol. 9, pp. 44 073–0002, 2004.

[151] R. Glardon, N. Karapatis, V. Romano, and G. Levy, "Influence of nd: Yag parameters on the selective laser sintering of metallic powders," *CIRP Annals*, vol. 50, no. 1, pp. 133–136, 2001.

[152] C.-Y. Ho, K.-M. Hung, M.-Y. Wen, and J.-E. Ho, "Thermal analysis of femtosecond laser processing for metal thin films," *Physica Scripta*, vol. 2010, no. T139, p. 014 005, 2010.

[153] T. Nagy, U. Pacher, A. Giesriegl, M. Weimerskirch, and W. Kautek, "Depth profiling of galvanoaluminium–nickel coatings on steel by uv-and vis-libs," *Applied Surface Science*, vol. 418, pp. 508–516, 2017.

[154] N. Nedialkov, S. Imamova, P. Atanasov, P. Berger, and F. Dausinger, "Mechanism of ultrashort laser ablation of metals: Molecular dynamics simulation," *Applied surface science*, vol. 247, no. 1-4, pp. 243–248, 2005.

[155] L. Ke, H. Zhu, W. Lei, and Z. Cheng, "Laser cleaning of rust on ship steel using tea co2 pulsed laser," in *Photonics and Optoelectronics Meetings (POEM) 2009: Industry Lasers and Applications*, International Society for Optics and Photonics, vol. 7515, 2009, 75150G.